Model study on particle size segregation and deposition during Asian dust events in March 2002

Zhiwei Han,[1,2] Hiromasa Ueda,[3] Kazuhide Matsuda,[1] Renjian Zhang,[2] Kimio Arao,[4] Yutaka Kanai,[5] and Hisashi Hasome[1]

[1] A size-segregated aerosol model that includes most of the major physical processes (generation, transport, and dry and wet deposition) is developed. This model is coupled with a Regional Air Quality Model (RAQM) and is applied to simulate Asian dust storms during the 10-day period of 15–24 March 2002. A nonhydrostatic mesoscale model (MM5) is used to provide meteorological fields. Model results are verified by available observational data including surface weather observations and size-segregated particle concentrations. The validation demonstrates a good capability of this model system in capturing most of the key features of dust evolution and reproducing the particle mass size distribution along the transport pathway of soil dust. An apparent feature has been both observed and reproduced by the model, showing a shift of size range with peak mass concentration from coarse mode to finer mode on the pathway from source regions to distant downwind areas. The maximum dust concentration averaged over 10 days is simulated to be 3000 μg m^{-3} over the southern China-Mongolia border. Total dry deposition of soil dust for 10 days is up to 30 g m^{-2} in the Gobi desert along the southern China-Mongolia border. Distribution and magnitude of particle deposition are strongly dependent on both concentration and size-segregated dry deposition velocity and scavenging rate. While dry deposition dominates the removal of dust particles in or in the vicinity of source regions, the influence of wet deposition increases along the transport pathway of soil dust, with high removal efficiency for coarser particles (>2 μm) and very low efficiency for particles in the accumulation mode. Of the total dust emission (43.2 megatons), about 71% is redeposited onto the underlying surface by the dry deposition process, 6% is removed by the wet deposition process, and the remaining 23% is suspended in the atmosphere or subject to long-range transport.   INDEX TERMS: 0305 Atmospheric Composition and Structure: Aerosols and particles (0345, 4801); 0322 Atmospheric Composition and Structure: Constituent sources and sinks; 0368 Atmospheric Composition and Structure: Troposphere—constituent transport and chemistry; 3210 Mathematical Geophysics: Modeling; KEYWORDS: Asian dust, aerosol model, particle size segregation, dry and wet deposition, dust budget

1. Introduction

[2] Asian soil dust originating from continental arid or semiarid areas has received much concern in the past 2 decades because of its significant influence on air quality, biogeochemical cycles, radiation balance, as well as Asian monsoon and climate changes [*Duce*, 1995; *Tegen and Fung*, 1994; *Zhang et al.*, 1998; *Sokolic et al.*, 1998]. A number of observations have been carried out to investigate the physical and chemical properties of soil dust aerosols [*Mori et al.*, 2002; *R. Zhang et al.*, 2003; *X. Zhang et al.*, 2003]. Numerical models with respect to soil dust aerosols have also been developed in recent years and have been utilized to study the deflation, transport, and budget of soil dust on a regional (East Asia) and a continental scale (from Asia to North America) [*Gong et al.*, 2003; *Shao*, 2001; *Shao et al.*, 2003; *Wang et al.*, 2000; *Park and In*, 2003; *Uno et al.*, 2001; *Liu et al.*, 2003; *Song and Carmichael*, 2001]. Much progress and success has been achieved in recent years from the above studies of dust-related topics. However, uncertainties still remain because of the deficiencies in our understanding of the behaviors of soil dust aerosol.

[1]Acid Deposition and Oxidant Research Center (ADORC), Niigata-shi, Japan.
[2]Institute of Atmospheric Physics, Chinese Academy of Sciences, Beijing, China.
[3]Disaster Prevention Research Institute, Kyoto University, Uji, Kyoto, Japan.
[4]Faculty of Environmental Sciences, Nagasaki University, Nagasaki, Japan.
[5]National Institute of Advanced Industrial Science and Technology, Tsukuba, Japan.

[3] Simulation of soil dust aerosol involves a series of complex processes including deflation, transport, dry and wet deposition, as well as potential heterogeneous reactions taking place on the aerosol surface. Among these processes, the removal process plays an important role in determining aerosol budget. It not only directly affects the residence time and evolutionary pattern of particles in the atmosphere, but also finally determines the sink of particles. The removal is also a very complex process, which is highly nonlinear, and size-dependent; for example, the dry deposition process is strongly dependent upon the meteorological condition, the underlying surface, as well as the property of particles [Sehmel, 1980; Chamberlain, 1983]. However, these processes are often simplified in previous studies; some semiempirical expressions or generalized formulas are applied to all particle size bins, and wet removal is just represented by a scavenging rate which is scaled to precipitation rate and is independent of size bins. Although the total dust mass load may be well simulated, some of the key features of the deposition process are inevitably lost [Giorgi, 1986]. As a result, uncertainties still remain in the current understanding of particle size distribution and budget. Therefore it is necessary to represent these deposition processes more realistically in the aerosol model for better understanding and further investigation of aerosol behaviors and budget.

[4] The size distribution property of aerosol determines its residence time in the atmosphere and is an important indicator in assessing the influence of aerosol on radiation and cloud processes. Aerosol removals by dry deposition and precipitation represent important processes, which dominate the size distribution and sink of aerosols. Deposition of soil dust can be tremendously enhanced during dust storm episodes and has large impacts on our social activity and ecosystem. Deposition of soil dust over oceans may provide abundant nutrients for phytoplankton that can release dimethyl sulfide (DMS), which in turn may serve as condensation nuclei of cloud and possibly be involved in a climate feedback loop [Charlson et al., 1987; Brasseur et al., 1999]. Because of the very dry air mass behind the cold front and the relatively small precipitation during dust episodes, especially over source regions, dry deposition is considered to dominate the total removal of dust particles, and wet deposition is often ignored or estimated by using the simple approaches mentioned above. Thus the wet deposition process during dust periods is still less understood. Recent work [Zhao et al., 2003] shows the significance of wet deposition on the transpacific transport pathway of Asian dust.

[5] Asian aerosols in springtime actually result from a combination of mineral soil dust, sea salt and anthropogenic sources. During the outbreak of a dust storm, soil dust aerosols take up most of the total mass loadings and have an overwhelming impact. Aerosols collected in coastal areas of Japan always show a high proportion of sea salt [Fujita et al., 2000]; the northwestern Pacific Ocean is thought to be a most important region of sea salt production and needs further investigation.

[6] In this study, an aerosol model is developed and utilized to study the transport and deposition processes of aerosols during the severe dust periods on 15–24 March 2002 in East Asia. Our focus is placed on (1) detailed validation of size-segregated mass concentrations, (2) investigation of the variability of particle mass size distribution along the transport pathway of soil dust, and (3) size-segregated dry and wet deposition flux, as well as dust mass budget. Quite a few observational data have been collected and used to evaluate the simulation results and model capability. The spatial distribution and magnitude of soil dust and sea-salt particles, the features in the size distribution of airborne particles, dry and wet depositions, as well as the dust budget in East Asia for a period of 15–24 March 2002 and during a severe dust storm on 19–23 March 2002 are simulated and analyzed in this study.

2. Model Description

[7] An aerosol model, which is fully size-dependent, has been developed in this study. It includes most of the key physical processes of aerosol: emission generation, transport and diffusion, and dry and wet removals. Dust emission plays an important role in dominating dust loading and depositions. Many studies have been conducted to improve the understanding of the mechanism of dust emission and to enhance the accuracy of dust emission prediction. There are presently two types of dust emission models used for dust transport simulation. The first type is a physically explicit model, which represents sophisticated mechanisms of dust production [Marticorena and Bergametti, 1995; Shao, 2001]. This type of model is physically sound and promising, but there are some difficulties in the application of this kind of model in East Asia because some of the basic parameters, such as particle size distribution for various erodible soil types, were unavailable until now. Another type of emission model is developed based on the analysis of physical and meteorological parameters in relation to dust mobilization using surface observations. For this approach, threshold values of friction velocity, soil or near-surface water content for various soil types have been investigated and used as key components for the initialization of dust deflation. This type of model is empirical or semiempirical, and it is relatively easier to apply in practice [Liu et al., 2003; Park and In, 2003].

[8] In this study, soil dust emissions are estimated mainly based on the approach of Gillette and Passi [1988]. Dust flux is calculated through the following formula:

$$F = C \times u_*^4 \left(1 - \frac{u_{*_t}}{u_*}\right) \times (1 - f_i Ri) \quad u_* \geq u_{*t}, \qquad (1)$$

where u_* and u_{*t} are the friction and threshold friction velocities and C is a constant (1.4×10^{-15}) which is calibrated from field studies by Gillette and Passi [1988]. Reduction factors are introduced, considering that dust emission can be reduced by vegetation cover in source regions [In and Park, 2002; Westphal et al., 1987]. R_i and f_i are the reduction factor and fractional coverage of i type of vegetation in a model grid. In this study, Ri is taken as 0.6 for grass, 0.7 for shrub and 0.1 for barren or sparsely vegetated land, derived from Park and In [2003].

Table 1. Particle Size Ranges and Mass Size Distributions of Vertical Dust Flux for Three Major Desert Regions of China Used in This Study

Bin	Size Range in Diameter, μm	Middiameters, μm	MSDs, %		
			AQJ	DH	ZBT
1	0.43–0.65	0.53	0.03	0.03	0.03
2	0.65–1.1	0.84	0.06	0.05	0.04
3	1.1–2.1	1.52	0.09	0.10	0.09
4	2.1–3.3	2.63	0.10	0.12	0.10
5	3.3–4.7	3.95	0.10	0.14	0.13
6	4.7–7.0	5.76	0.11	0.15	0.19
7	7.0–11.0	8.85	0.08	0.18	0.22
8	11.0–17.5	14	0.11	0.09	0.05
9	17.5–27.0	21.5	0.14	0.06	0.07
10	27.0–42.0	34	0.18	0.08	0.08

Fractional coverage for each grid is obtained from the U.S. Geological Survey (USGS) satellite data with a horizontal resolution of 5 min. Land use data are derived from Normalized Difference Vegetation Index (NDVI) retrieved land cover classification by *Defries and Townshend* [1994]. Three major categories of bare ground, bare ground with little shrubs and plain with low grass in this data set represent most of the arid and semiarid areas in East Asia. Erodible areas are further identified in terms of the soil maps used in *Gong et al.* [2003] and *Park and In* [2003]. Dust deflation is confined to erodible areas. The threshold friction velocities above which dust deflation initiates are chosen as 0.4, 0.5, and 0.65 m s^{-1} for the three categories of source regions mentioned above, based on previous studies and analysis of sensitivity model simulations [*Gillette and Passi*, 1988; *Westphal et al.*, 1988; *In and Park*, 2002]. The occurrence frequency of dust deflation has been found to apparently decrease with increasing relative humidity [*Wang et al.*, 2000; *Park and In*, 2003]. This implies that relative humidity could be taken as an indicator for dust deflation in Asian source regions. In this study, dust deflation is allowed in source regions when near-surface relative humidity is less than the upper limits, which are 0.5, 0.5, and 0.4 for the above three categories of source regions. Coagulation is not included in the current aerosol model because it is not an important process during dust periods when larger particles dominate [*Westphal et al.*, 1988; *Song and Carmichael*, 2001; *In and Park*, 2002].

[9] In this study, particles with diameter ranging from 0.43 to 42 μm are grouped into 10 size bins in terms of the eight stages of aerosol sampler, with three additional size bins above 11 μm for larger particles. Table 1 lists the particle size ranges in this study. The size distribution of dust emission is an important parameter in achieving a soil dust simulation. In this study, the total dust emission flux is apportioned to each size bin based on the up-to-date observational findings on the size distribution of vertical dust flux from Chinese major source regions during the Aerosol Characterization Experiment–Asia (ACE-ASIA) which was carried out in spring 2001 [*X. Zhang et al.*, 2003]. A lognormal fit was found in the size distribution of vertical dust flux between 0.25 μm and 16 μm through the analysis of a series of measurements. Table 1 presents mass

size distributions (MSDs) (in percentage) of vertical dust flux for three major desert regions: AQJ (Arksu, Qira, and Jartai), DH (Dunhuang), and ZBT (Zhenbeitai). MSDs are assigned to total dust emission in each source region according to their locations.

[10] The generation of sea-salt aerosols is estimated by using the formula of *Monahan et al.* [1986] in which both bubbles and spume mechanisms are included. The flux, which represents sea-salt droplet generation rate from bubble per unit area of sea surface, per increment of droplet radius, is given by (r < 10 μm)

$$\frac{dF_0}{dr} = 1.373 \, U_{10}^{3.41} r^{-3} \left(1 + 0.057 \, r^{1.05}\right) \times 10^{1.19 e^{-B^2}},$$

$$B = \frac{0.380 - \log r}{0.650}, \tag{2}$$

where r is droplet radius and U_{10} is the wind speed at 10 m. The spume mechanism has not been used because it tends to overpredict the flux for larger particles (r > 10 μm). Sea-salt particle is divided into eight size bins in accordance with the first eight bins in Table 1. In the size range 0.43–17.5 μm, sea-salt generation is dominated by indirect mechanism (via bubbles).

[11] Dry deposition velocity is represented by size-dependent parameterizations in this model with respect to different categories of underlying surface. Dry deposition velocity of particle is expressed as the inverse of the sum of resistant plus a gravitational settling term:

$$V_d = \frac{1}{r_a + r_b + r_c} + V_g, \tag{3}$$

where r_a is aerodynamic resistance above canopy, r_b is quasi-laminar layer resistance, r_c is surface resistance, which is assumed to be zero, and 100% capture by surface for particles. Gravitational settling velocity is calculated as:

$$V_g = \frac{d_p^2 \rho_p g C}{18 \mu}, \tag{4}$$

where d_p and ρ_p are the diameter and density of particle, respectively, μ is air dynamic viscosity, g is the gravitational acceleration, and C is slip correction factor, which is expressed as:

$$C = 1 + \frac{2\lambda}{d_p} \left(1.257 + 0.4 e^{-\frac{1.1 d_p}{2\lambda}}\right), \tag{5}$$

where λ is the mean free path of air molecule. The aerodynamic resistance r_a is calculated by

$$r_a = \frac{\ln(Z_r/Z_0) - \psi_\eta}{k u_*}. \tag{6}$$

Here Z_r is set as the height of first model layer, Z_0 is roughness length, ψ_h is the similarity function for heat, k is Von Karman constant, and u∗ is the friction velocity.

[12] Quasi-laminar resistance r_b is largely dependent upon Brownian diffusion, interception, and impaction. Parameterizations on three major categories of land use (smooth land,

vegetative and water surface) are considered in this aerosol model to realistically represent dry deposition process. For smooth surfaces, which are represented by ice, snow, desert or bare soil. r_b is calculated based on the approaches of *Seinfeld and Pandis* [1998]:

$$r_b = \frac{1}{u_*(Sc^{-2/3} + 10^{-3/St})}, \tag{7}$$

where u_* is the friction velocity, $Sc = \nu/D$ is Schmidt number, St is the Stokes number, and here $St = u_*^2 v_g/g\nu$ [*Giorgi*, 1988]. ν is kinematic viscosity of air, and D is Brownian diffusivity coefficient. For vegetative surfaces (forest, crop, grass, mixing woodland, etc), we adopt the scheme of *Zhang et al.* [2001] which is developed based on the work of *Slinn* [1982]:

$$r_b = \frac{1}{\varepsilon_0 u_*(E_b + E_{im} + E_{in})R}. \tag{8}$$

E_b, E_{im} and E_{in} are the collection efficiencies from Brownian diffusion, impaction and interception, respectively, ε_0 is an empirical constant, and R is the fraction of particles sticking to the surface, representing bound-off of coarse particles. Detailed description can be found in *Zhang et al.* [2001]. Bounce-off of particles for dry underlying surfaces is accounted based on the expression suggested by *Slinn* [1982]:

$$R = e^{-St^{1/2}}. \tag{9}$$

No particle rebound from wet or water surface is assumed. Over sea or ocean surfaces, the quasi-laminar boundary layer (QBL) is supposed to be disrupted by bursting bubbles, resulting in an increase in downward movement of particles. We use the approach of *van den Berg et al.* [2000] in which resistance r_b is determined by Brownian diffusion and impaction when the QBL is intact, and by turbulence and the washout velocity of particles by spray drops when the QBL is broken down:

$$r_b = \frac{1}{(1 - a_{bb})(V_b + V_i) + a_{bb}(V_a + V_w)}, \tag{10}$$

where a_{bb} is the relative area with bursting bubbles, V_b is Brownian diffusion velocity, V_i is impaction velocity, V_w is the washout velocity, and $V_a = 1/r_a$.

$$V_b = \frac{Cu_*}{\sqrt{Sc}\, \text{Re}}, \tag{11}$$

where Re is the Reynolds number ($Re = u_*Z_0/\nu$) and C is a constant ($=1/3$).

$$V_i = u_* 10^{-3/St} \tag{12}$$

$$V_w = E_c(2\pi r_{sd}^2)(2Z_{sd})F_{sd}, \tag{13}$$

where E_c is the collection efficiency ($=0.5$) of the spray drops, $2\pi r_{sd}^2$ is the area of spray drops, Z_{sd} is the average height reached by spray drops ($=50$ m), and F_{sd} is the flux of

spray drops ($=500 \times 10^4$ m^{-2} s^{-1}). The area of bursting bubbles a_{bb} can be approximated by the area covered with whitecaps, which is

$$a_{bb} = 1.7 \times 10^{-6} u_{10}^{3.75}, \tag{14}$$

where u_{10} is the wind speed at 10m heights.

[13] Below-cloud scavenging (BCS) of particles between cloud base and ground surface plays an important role in wet removal process. In-cloud removal process is not taken into account in this version of aerosol model with respect to its very small contribution to total wet removal of particles ($r > 0.5$ μm) [*Gong et al.*, 1997a, 1997b]. BCS is parameterized based on the expression of scavenging rate of *Slinn* [1984] as follows:

$$\psi(r_i) = \frac{cp\overline{E}(r_i, R_m)}{R_m}, \tag{15}$$

where p is precipitation rate (mm h^{-1}) and $\overline{E}(r_i, R_m)$ is the mean collision efficiency of particle by hydrometeor, which can be calculated by the following expression:

$$E = \frac{4}{\text{Re}\,Sc}\left(1 + 0.4\,\text{Re}^{1/2}Sc^{1/3} + 0.16\,\text{Re}^{1/2}Sc^{1/2}\right) + 4K$$
$$\cdot \left[\omega^{-1} + \left(1 + 2\,\text{Re}^{1/2}\right)K\right] + \left(\frac{St - S_*}{St - S_* + 2/3}\right)^{3/2} \tag{16}$$

$$S_* = \frac{12/10 + (1/12)Ln(1 + \text{Re})}{1 + Ln(1 + \text{Re})}, \tag{17}$$

where Re is the Reynolds number of hydrometeors, Sc and St are Schmidt and Stokes numbers of particles, and here $Sc = \nu/D$, $St = \tau(v_t - v_g)/R_m$. τ is the characteristic relaxation time of the particles. v_t and v_g are terminal velocity of hydrometeors and particles. $K = r_i/R_m$, r_i and R_m are radius of particles and hydrometeors. $\omega = \mu_w/\mu_a$, μ_w and μ_a are the viscosity of water and air, respectively. Parameterization of below-cloud scavenging described above includes the main capture processes of aerosol by falling hydrometeor through Brownian and turbulent shear diffusion, interception and inertial impaction.

[14] The aerosol model is embedded into a Regional Air Quality Model (RAQM) to solve transport and diffusion processes. RAQM utilizes a spherical terrain-following sigma coordinate. An accurate mass conservative, peak-preserving algorithm is used to solve a three-dimensional mass conservative equation with a time-splitting method [*Carmichael et al.*, 1986; *Walcek and Aleksic*, 1998]. The vertical eddy diffusivity is parameterized in terms of the approach of *Byun and Dennis* [1995], which has been used in a Regional Acid Deposition Model version 2.6 (RADM 2.6). RAQM has been used to study the impacts of volcanic emissions on sulfur oxides [*An et al.*, 2003].

[15] A nonhydrostatic, fifth-generation mesoscale model (MM5) is applied to drive the air quality model. It provides meteorological fields including wind, temperature, humidity, surface pressure and other surface parameters. The FDDA technique is used in running MM5. Several main physical processes are parameterized by specific options
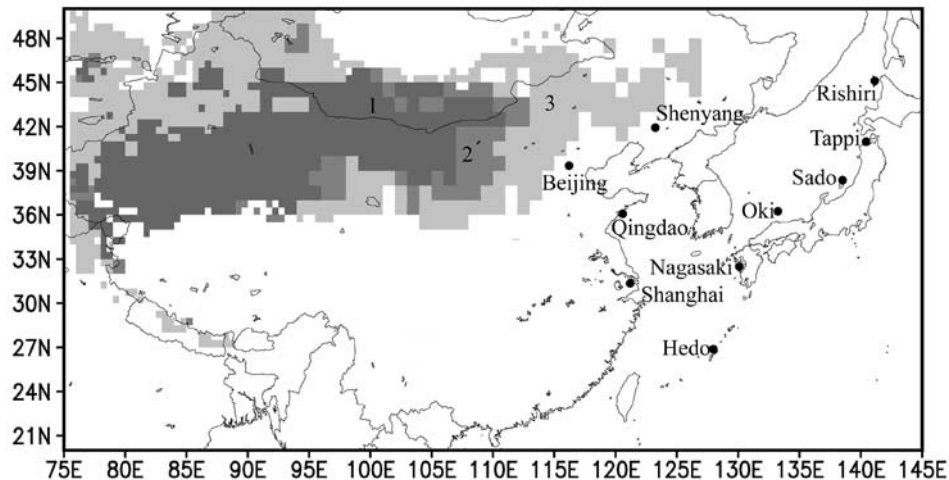
Figure 1. Soil dust source regions in the model domain and specific monitoring sites.

such as the MRF scheme for the boundary layer, the Kain-Fritsch scheme for convective motion, the cloud cooling scheme for radiation, etc. NCEP reanalysis data, four times a day with $1° \times 1°$ resolution, are used for initial and boundary conditions. Twenty-three levels are unequally distributed in vertical direction from ground to 100 hPa level, whereas horizontal resolution is selected as 50 km. MM5 outputs are appropriately interpolated from Lambert projection to spherical coordinate of RAQM.

3. Model Parameters and Observational Data

[16] The model domain for this study is from 75° to 145°E, and 20° to 50°N, including almost all desert regions in East Asia. Figure 1 shows the modeling domain, major dust source regions and monitoring sites in this study. The horizontal grid resolution of air quality model is $0.5° \times 0.5°$. Twelve vertical layers stretch unequally from the ground to 10 km with the first half layer being 50 m above ground. Three-day initialization prior to formal integration is carried out with initial dust concentration being zero. The formal integration period is from 15 to 24 March 2002. Anthropogenic primary emission of PM_{10} has been also taken into account in simulation to provide a background aerosol concentration from anthropogenic origin. The human-induced PM_{10} emission for the year 2000 with $0.5° \times 0.5°$ resolution is derived from the Center for Global and Regional Environmental Research (CGRER). This emission rate is distributed to each size bin according to the observed evidence of mass size distribution of airborne aerosol during a nondust period in March 2002.

[17] Various observational data are used to verify the spatial distribution, temporal variation, as well as mass size distribution of particles. These data include surface station weather observations from the World Meteorological Organization (WMO) SYNOP bulletins, PM_{10} concentrations at four big Chinese cities derived from the State Environmental Protection Administration (SEPA) of China, PM_{10} and $PM_{2.5}$ concentrations at five remote monitoring sites of the Acid Deposition Monitoring Network in East Asia (EANET), mass size distribution of aerosol collected by

Andersen sampler at Beijing and Qingdao, China, and particle number concentration measured by optical particle counter (OPC) at Nagasaki, Japan. An Andersen sampler (AN-200) manufactured by Shibata Scientific Co., Ltd., was employed to collect size-separated particles at both Beijing and Qingdao. The flow rate was maintained at 28.3 L min^{-1} to achieve ideal size separation. The Andersen sampler has eight cutoff diameters of 11, 7.0, 4.7, 3.3, 2.1, 1.1, 0.65, and 0.43 μm. PF050 ployflon filter (Advantec Co., Ltd.) and 2500QAT-UP quartz filter (Tokyo Dylec Co., Ltd.) were used in AN-200. The sampling site at Beijing is on the top of a two-story building (8 m above ground) which is 50 m west of the 325 m Meteorological Tower (116°22′E, 39°58′N). Qingdao is a coastal city on the major transport pathway of soil dust from the continent to the western Pacific Ocean. The sampler is placed on the roof of a three-storey building of Ocean University of China (120°19′E, 36°06′N). This building is located on a small hill near the seashore, with the altitude of 65 m above the ground. An optical particle counter (RION, KC-01B) was used to measure number size distribution of particles at Nagasaki University (129.9°E, 32.8°N). KC-01B has five channels with size ranges of 0.3–0.5, 0.5–1.0, 1.0–2.0, 2.0–5.0 and >5.0 μm in diameter. The aerosol index from the Total Ozone Mapping Spectrometer (TOMS) is one of the data sets for model results evaluation, but the quality of TOMS data for this period is so poor that extreme dust deflation processes over Asian source regions cannot be retrieved [*Shao et al.*, 2003]; thus we do not use this data set for model validation.

4. Model Validation and Results

### 4.1. Review and Validation of Soil Dust Fluxes With Surface Dust-Rise Observations

[18] In March 2002 there are two nearly consecutive dust storms that have been clearly documented in downwind areas. Figure 2 presents a time series of surface PM_{10} concentrations at the Sado-seki monitoring site, Japan, where two dust storms on 18 March and 22 March are clearly displayed. Figure 3 shows the spatial distribution
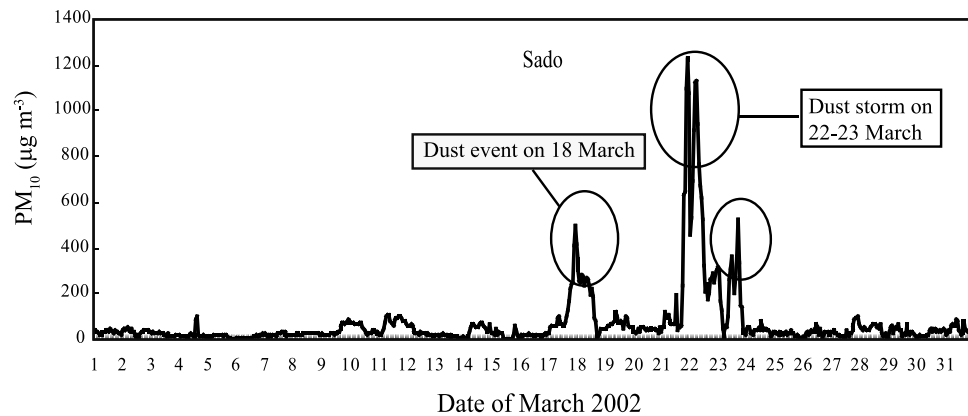
Figure 2. Time series of observed PM_{10} concentrations at the Sado site of Japan in March 2002.

and temporal evolution of dust emission fluxes, 10m wind vectors, as well as observed dust-rises at or near the weather stations, derived from WMO 6 hourly surface weather observations. The first dust storm was initiated from the southeastern China-Mongolia border on 15 March (Figure 3a) and lasted about 2 days, mainly influencing northern and eastern parts of China and portions of the western coast of Japan. Dust-rise was also observed and predicted in the western Kumtag desert. Another evident

dust deflation process was initiated around 1200 LST 16 March 2002 from western Inner-Mongolia (near 98°E, 39°N), with dust flux exceeding 2500 μg m^{-2} s^{-1}, influencing several downwind cities such as Lanzhou and Xinin where severe degradation of air quality was reported. Owing to the anticyclonic southeastward transport pattern, this dust storm just affected certain regions west of China, and it was mostly a localized dust storm. The second dust storm was regarded as the strongest dust storm within the past decade in terms of the
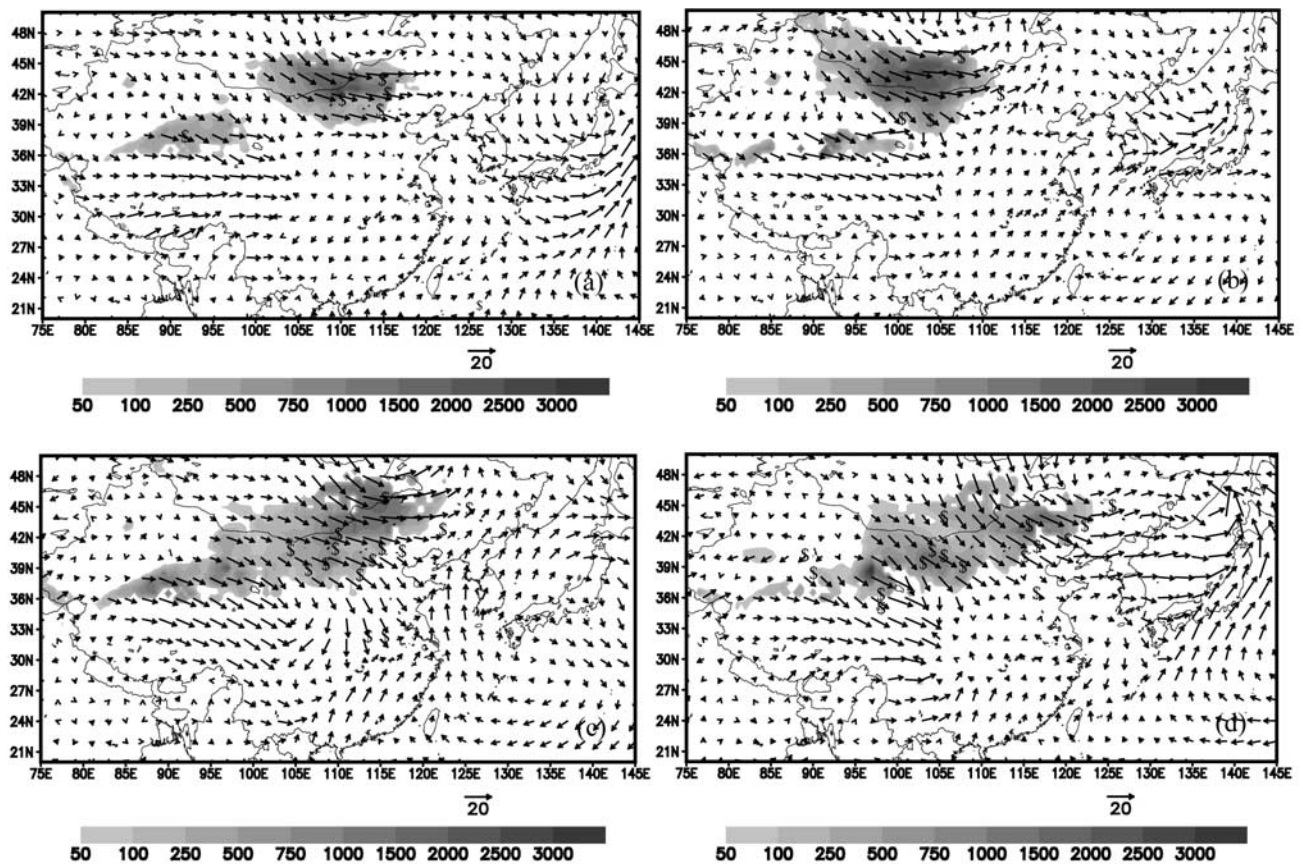
Figure 3. Soil dust fluxes (μg m^{-2} s^{-1}) and 10 m wind vectors (m s^{-1}), and observed dust-rise (denoted by dollar signs, from WMO surface weather stations) at (a) 0600 UTC 15 March, (b) 0600 UTC 19 March, (c) 0600 UTC 20 March, and (d) 0600 UTC 21 March.

magnitude of dust concentration in downwind areas. It swept over most parts of China, with its evident influence reaching Shanghai, and even some portions of southern China. Broad downwind areas including the Korean peninsula, Japan and the western Pacific Rim experienced abrupt and tremendous elevation of aerosol concentrations under the prevailing eastward continental outflow. This dust storm originated from the Gobi desert near the southern China-Mongolian border on 19 March (Figure 3b) associated with a strong cold front moving southeastward. Soil dust was reuplifted over the southeastern China-Mongolia border on 20 March (Figure 3c). On 21 March, major dust generation occurred over semiarid areas north of Beijing and Shanxi province (Figure 3d), northern Inner-Mongolia, the eastern part of the Kumtag desert, as well as the southern fringe of the Taklimakan desert, affecting a large portion of northern China, a part of western China and the whole Korean peninsula. In general, modeled dust deflation shows a good agreement with reported dust-rise in terms of spatial distribution and temporal evolution, except for some isolated areas in northeastern and central China where soil sources are mostly localized. During this period, dust deflation is much lower in the Taklimakan desert than in other major source regions of East Asia.

[19] Dust emission of this study shows a general agreement with that of *Park and In* [2003] for the second dust storm period (19 to 23 March). Location and timing of dust deflation are quite similar, in particular, dust-rise in semiarid areas north of Beijing on 21 March are well reproduced by both models. However, there are relatively large differences for the intensity of dust emission. The maximum of dust emission predicted by *Park and In* [2003] reaches 12,000 $\mu g\ m^{-2}\ s^{-1}$ in mixed soil regions on 19 March, whereas the maximum in this study is about 3,500 $\mu g\ m^{-2}\ s^{-1}$ in the Gobi desert of southern Mongolia. *Shao et al.* [2003] conducted a real-time numerical prediction of Asian dust over a domain similar to this study for March and April 2002. In most cases, our predicted dust emissions are consistent with *Shao et al.* [2003]. Both models have predicted major dust deflations over southern Mongolia and northern Inner-Mongolia on 19 March, the southeastern China-Mongolia border on 20 March, north of Beijing, western Inner-Mongolia (Badain Juran, Tengger and Ulan Buh desert) and the eastern Kumtag desert on 21 March. However, the dust emission in the Tulufan basin on 19 March appears to be underpredicted in this study, probably due to the inaccuracy of land use and inadequate threshold values selected to initialize dust-rise for that region. Differences also exist over western isolated regions for weak dust-rise cases. For the second dust storm, the maximum of dust flux of this study (3,500 $\mu g\ m^{-2}\ s^{-1}$) is similar to the results of *Shao et al.* [2003] in which the maximum dust emission reaches 5,000 $\mu g\ m^{-2}\ s^{-1}$ over the Gobi desert. In summary, dust emission predicted by our model system shows a reasonable agreement with reported dust-rise record, and is generally consistent with previous studies.

4.2. Validation of Soil Dust Concentrations With Surface Visibility Observations

[20] Figure 4 shows the corresponding evolutionary pattern of total soil dust concentrations and visibility (unit in kilometer) derived from WMO 6 hourly surface weather observations. Visibility less than 5 km was used to identify the main body of dust plumes. Figure 4a shows that the strong dust deflation around the southern China-Mongolia border results in very high dust concentration in southern Mongolia and western Inner Mongolia at the beginning of the second dust storm, with a maximum reaching 20,000 $\mu g\ m^{-3}$ (Figure 4b). At the same time, large areas of western source regions experience a high level of airborne particles as well, such as the Kumtag desert, southeastern portions of the Taklimakan desert, as well as portions of the Tulufan and Zhunge'er basin. The dust storm spreads widely and is transported eastward and southeastward following the synoptic flow; it is refilled by dust emissions over the southeastern China-Mongolia border on 20 March, with dust concentration exceeding 10,000 $\mu g\ m^{-3}$ along the border (Figure 4c). On 21 March, dust concentration in semiarid areas north of Beijing is significantly elevated due to a strong deflation process there. High concentration centers also occur in western Inner-Mongolia (Ulan Buh desert) and the Kumtag desert, resulting from large dust emissions in those regions (Figure 4d). Modeled dust concentration agrees with observed visibility quite well in terms of spatial pattern, temporal variation and intensity with the exception of western portions of the Taklimakan desert and the Tulufan basin where the model appears to underpredict observation on 21 March and 19 March.

[21] Figure 5 presents the evolutionary images of daily averaged near-surface dust concentrations, related to the two dust storms mentioned above. Comparison with results of *Shao et al.* [2003] shows similarities both in spatial pattern and magnitude for dust evolutions. Apart from high dust concentrations over major source regions, such as southern Mongolia, northern Inner-Mongolia and semiarid areas north of Beijing have been well reproduced by both models; two high dust centers in western Inner-Mongolia and the eastern Kumtag desert on 21 March, and a large dust cloud over central China (around 105°E, 36°N) on 22 March, are similarly predicted by both models as well. However, our results show higher dust concentrations in the southern Taklimakan desert and the Kumtag desert on 19 and 20 March, and lower dust level in portions of the Tulufan and Zhunge'er basin, compared with the work of *Shao et al.* [2003].

4.3. Validation With Surface Observation of PM_10 and PM_2.5 From SEPA and EANET
4.3.1. API and PM_10

[22] Air Pollution Index (API) from SEPA is a result of spatial and daily average of observational data at a number of monitoring sites in big cities of China. It reflects a mixture of aerosol from all kinds of sources including anthropogenic emissions. PM_{10} concentration can be deduced from API through a standard formula prescribed by SEPA. Generally, the data in urban background are not suitable for validation due to the coarser grid resolution in regional models. However, such comparison becomes reasonable when dust storms occur because mineral dust has an overwhelming influence even in urban areas and urban
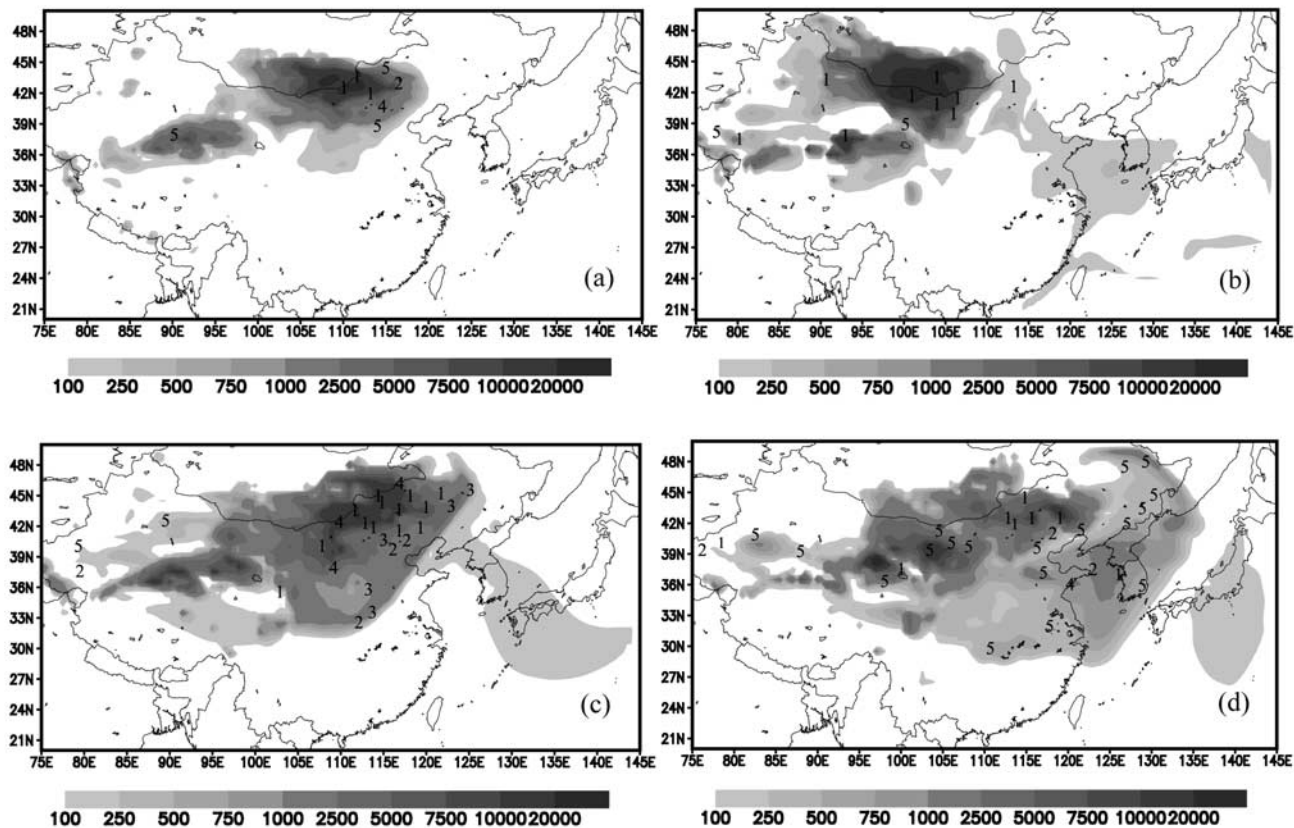
Figure 4. Total soil dust concentrations ($\mu g\ m^{-3}$) and observed visibility (denoted by numbers 1–5 in kilometers, from WMO surface weather stations) at (a) 0600 UTC 15 March, (b) 0600 UTC 19 March, (c) 0600 UTC 20 March, and (d) 0600 UTC 21 March.

aerosols tend to reflect more regional features duirng dust periods than in nondust days. Therefore such a data set provides a good database in the evaluation of model performance over the continent. Figure 6 shows the time series of simulated and observed daily average PM_{10} concentrations at four representative Chinese megacities (Shenyang, Beijing, Qingdao, and Shanghai) from 15 to 24 March 2002. (It needs to be clarified that the daily average value in Figure 6 represents a 1-day period starting from 1200 BJT (UTC + 8 hours), in accordance with the calculation method of API prescribed by SEPA.) Anthropogenic emissions in Chinese big cities are adjusted by multiplying a factor of 2 based on the fact that 30–70% of particulate matter in Chinese urban areas originated from exposure land surface (including construction fields), especially in northern China [*Wang and Wang*, 1996; *Shao et al.*, 1995]. Figure 6 shows that the present model reasonably reproduces two dust events at four cities. Two peaks caused by dust storms are well captured by the model. In Figure 6, 600 $\mu g\ m^{-3}$ at Beijing on 16 and 21 March indicates that observed daily average PM_{10} concentration exceeds 600 $\mu g\ m^{-3}$, which is the upper limit of API. Simulations match observations quite well at Qingdao and Shanghai, but the value at Shenyang on 21 March seems to be overpredicted. In general, the model reproduces well the PM_{10} concentrations during and between the two dust storms at the above four cities; both simulation and observation show

that the influences of these two dust storms reach as far as Shanghai in China.

[23] EANET is an intergovernmental organization, which is dedicated to investigating acid deposition and air quality and to evaluating their impacts on the atmosphere and ecosystems in East Asia (see http://www.adorc.gr.jp/eanet.html). It has 12 participating countries from East Asia at present. From the year 2001, EANET starts its regular phase. QA/QC (quality assurance and quality control) activities are conducted to ensure high quality of monitoring data. In this study, five remote monitoring sites spreading from north to south (Rishiri, Tappi, Sado-seki, Oki, Hedo) along the western coast of Japan and the western Pacific Rim are chosen for validation. First, model capacity in modeling sea-salt aerosols is verified. We try to look for the clean background air mass to avoid possible influence from the continent. Nearly 36 hours with north or northwest wind were selected from 0000 UTC, 20 March to 1200 UTC, 21 March 2002. After 1700 UTC 21 March, wind direction began to change to the southwest, followed by the arrival of a cold front and continental dust aerosols. Figure 7a illustrates the backward trajectories starting from the altitude of 300m over Rishiri site; it shows that the air parcels to the Rishiri site during this period mainly come from the north of Russia which is normally regarded as relatively clean background. The high correlation between wind speed and PM_{10} concentration and increasing Na^{+} concentration in precipitation also support that sea salt
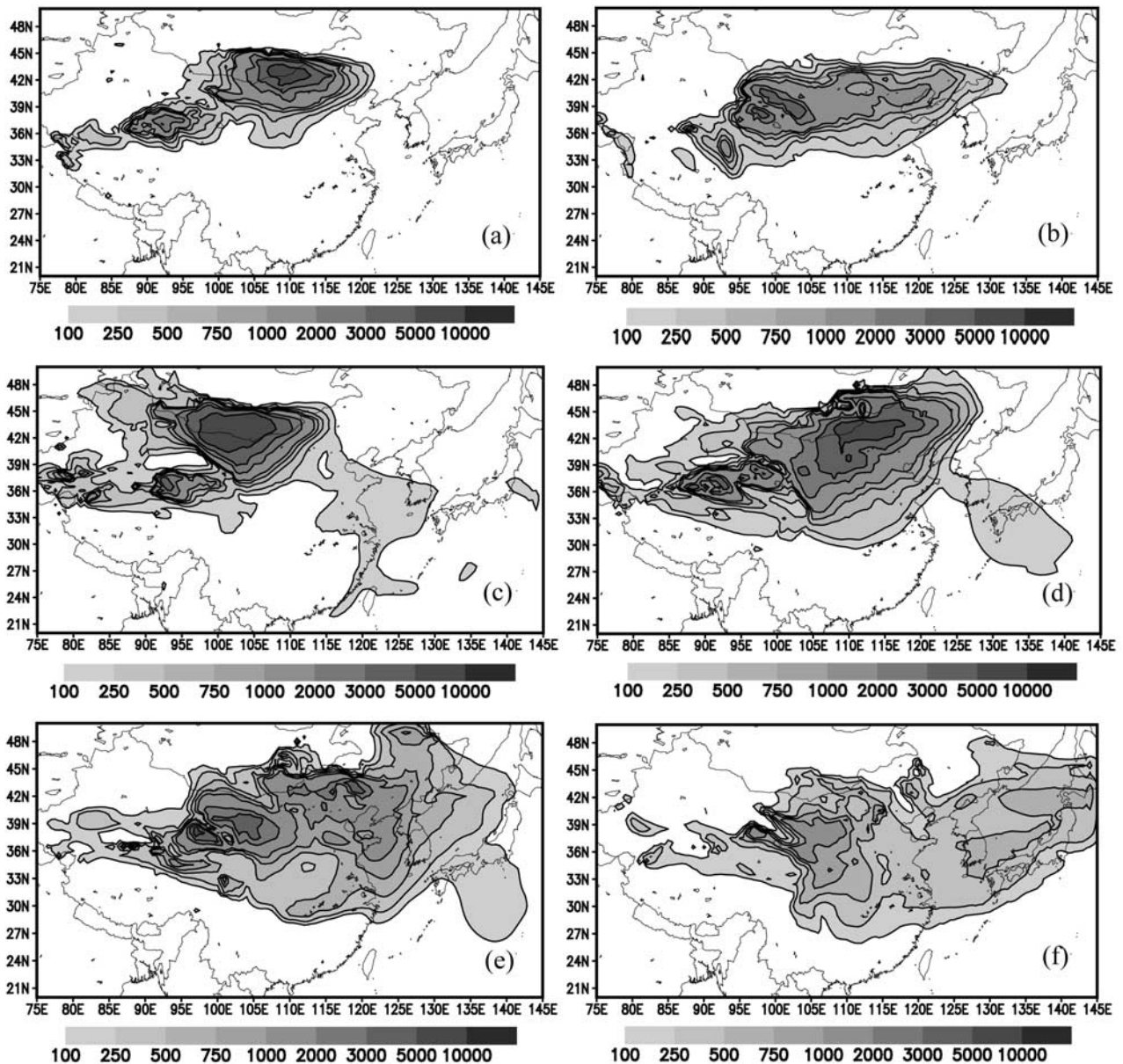
Figure 5. Model simulated daily averaged near-surface dust concentrations (μg m^{-3}) for (a) 15, (b) 16, (c) 19, (d) 20, (e) 21, and (f) 22 March 2002.

could be the dominant component for this period. Figure 7b illustrates a time series of hourly observed and simulated PM_{10} concentrations. Simulations agree quite well with observations, indicating the good capability of this aerosol model in reproducing major physical features of sea-salt aerosols.

[24] Figure 8 presents the simulated and observed daily average PM_{10} concentrations at five coastal sites of Japan. The simulated PM_{10} concentration here represents the sum of particles coming from different source origins of soil dust, sea-salt and anthropogenic emissions. Soil dust particle shown in the figure includes a small proportion of particles from anthropogenic origin, which cannot be clearly displayed because of its very small percentage of total mass loading during dust episodes. The observed peaks caused by first dust storm are clearly reflected at Oki on 17 March and

at Sado-seki on 18 March. The model correctly captures these two peaks, with very good simulation at the Oki site. The second peak is both observed and reproduced on 22 March at all the sites except for Hedo. Extremely high daily average PM_{10} concentrations exceeding 600 μg m^{-3} appear at the Tappi and Oki sites. The simulated maxima at the Oki, Sado-seki and Rishiri sites agree quite well with observations. At the Tappi site the model tends to underpredict the observed values by a factor of 2 on 23 March, probably due to the inaccuracy in meteorological fields or uncertainties in dust emission from source regions. The model reasonably reproduces the day-to-day variation of aerosol concentration at the Hedo site, but overprediction is found clearly for both dust and sea-salt aerosols on 23 and 24 March, mainly due to the underprediction of precipitation at the Hedo site, or other potential uncertainties result-
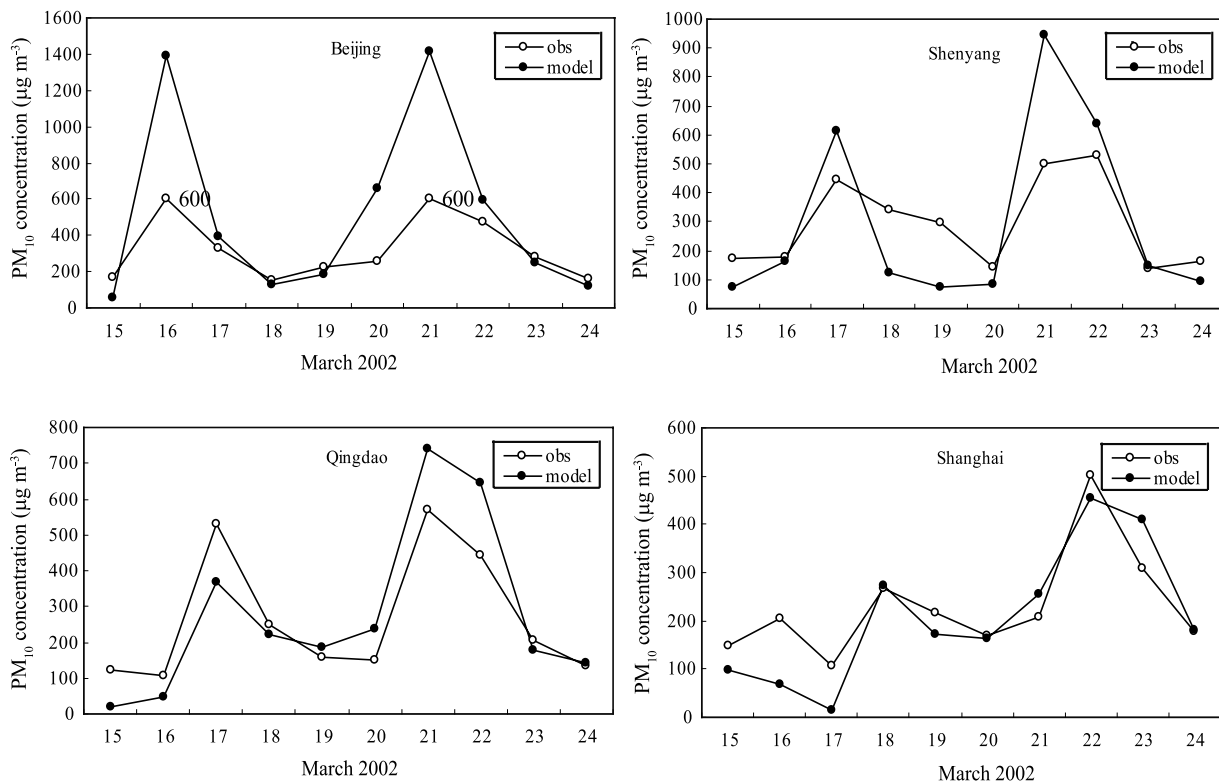
Figure 6. Simulated and observed daily average PM$_{10}$ concentration (μg m^{-3}) at four big cities in China.

ing from the overestimation of sea-salt production near Hedo or overprediction of dust particles along the transport pathway.

[25] Figure 9 shows the time series of simulated and observed hourly PM$_{10}$ concentrations at the Rishiri and Sado-

seki sites. The starting and ending times of dust storms simulated by the model accord with observation very well at both of two sites. Model prediction for the first peak at Sado-seki is excellent, with little difference in absolute value. The peak resulted from the second dust storm at
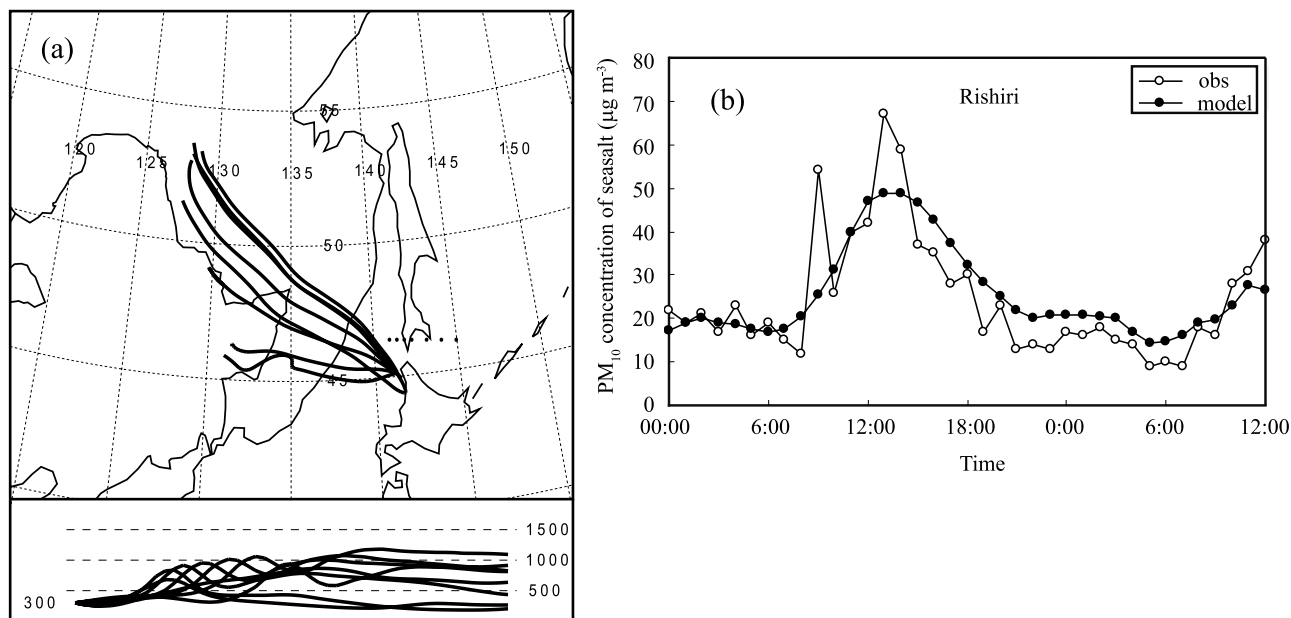
Figure 7. (a) Backward trajectories calculated every 3 hours, starting from the height of 300 m over Rishiri and (b) the time series of simulated and observed hourly PM$_{10}$ concentration (μg m^{-3}) from 0000UTC 20 March to 1200UTC 21 March 2002 at the Rishiri site.
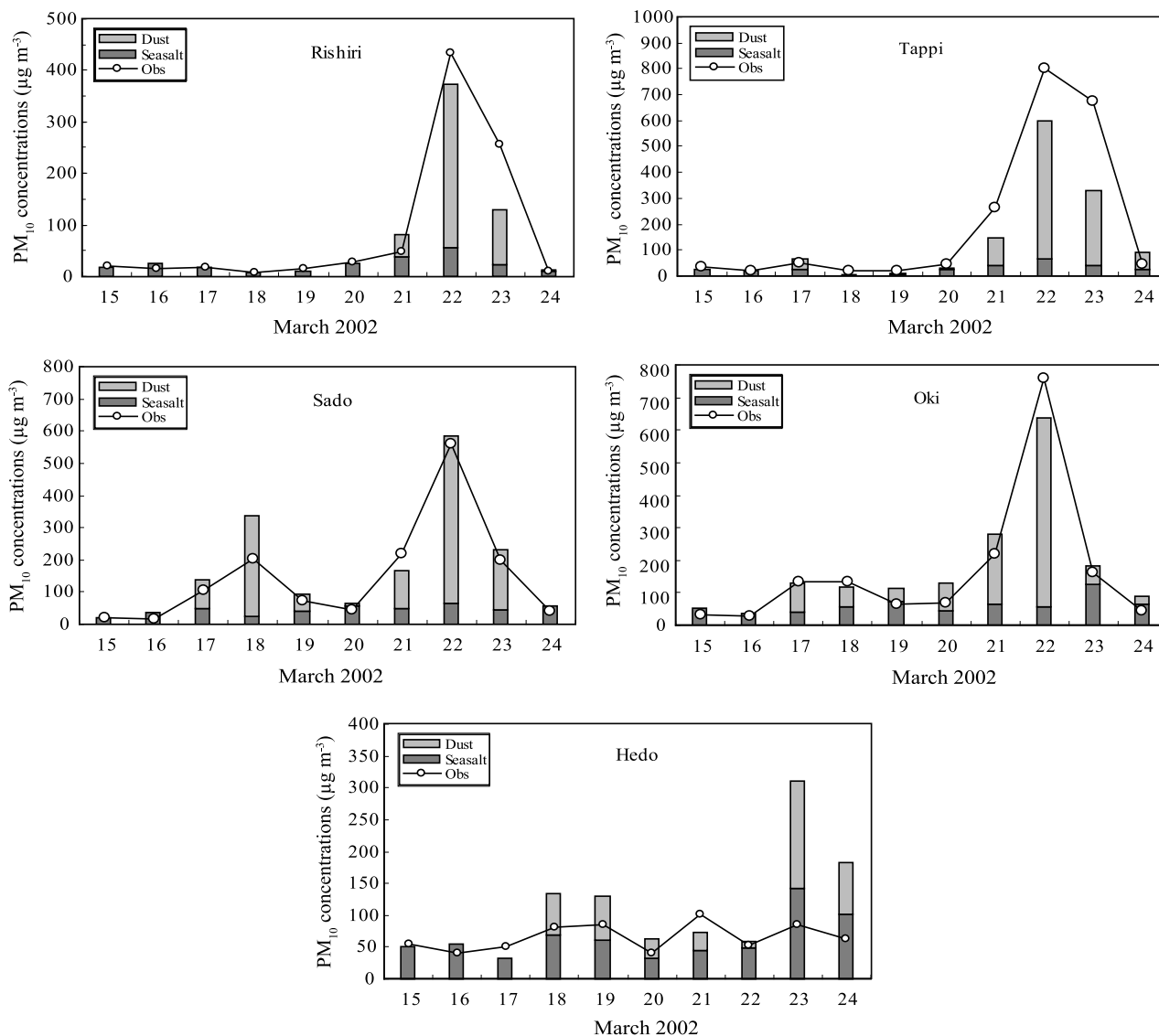
Figure 8. Simulated and observed daily average PM_{10} concentrations ($\mu g\ m^{-3}$) at five remote monitoring sites in Japan.

Sado-seki is also reasonably reproduced except that the simulation is somewhat lower than observation. At the Rishiri site, high concentrations caused by the second dust storm around the midnight on 22 March are successfully simulated. The model also reproduces well the two peaks on 16 March and 20 March 2002, resulting from remarkable increasing of sea-salt aerosol production.

4.3.2. $PM_{2.5}$

[26] Fine particles are of great concern because of their great harm to human health and their important implications to radiation and cloud processes. Figure 10 shows the simulated and observed daily average $PM_{2.5}$ concentration at the Oki and Rishiri sites. In Figure 10, total particle mass loadings are represented by the sum of particles from mineral dust, sea-salt and anthropogenic origin. Proportions of particles from sea-salt and anthropogenic primary emission are also illustrated. Simulated $PM_{2.5}$ shows a general good agreement with observation, especially for dust periods. At the Oki site, two peaks (on

17 March and 21–23 March 2002) resulting from transport of mineral dust have been well simulated, consistent with the good model performance for PM_{10}. The model also has a good result at the Rishiri site for the period of 21–23 March when dust storm prevails. However, it is noticeable that during nondust periods, simulation is apparently lower than observation. At the Oki site, simulated $PM_{2.5}$ concentrations are about 2 times lower than observed ones on 15–16 March. At the Rishiri site the discrepancy is about a factor of 4 on 15–19 March. These differences are suggested as mainly attributable to the uncertainties from anthropogenic origins. It is known that anthropogenic aerosol emissions generally have a larger proportion in finer mode compared with mineral dust. Moreover, fine particles in the range 0.1–2 μm have the smallest dry deposition velocity and smallest collision efficiency between falling raindrop and particles [*Giorgi*, 1986; *Andronache*, 2003]. These properties result in low removal efficiency of both dry and wet deposition pro-
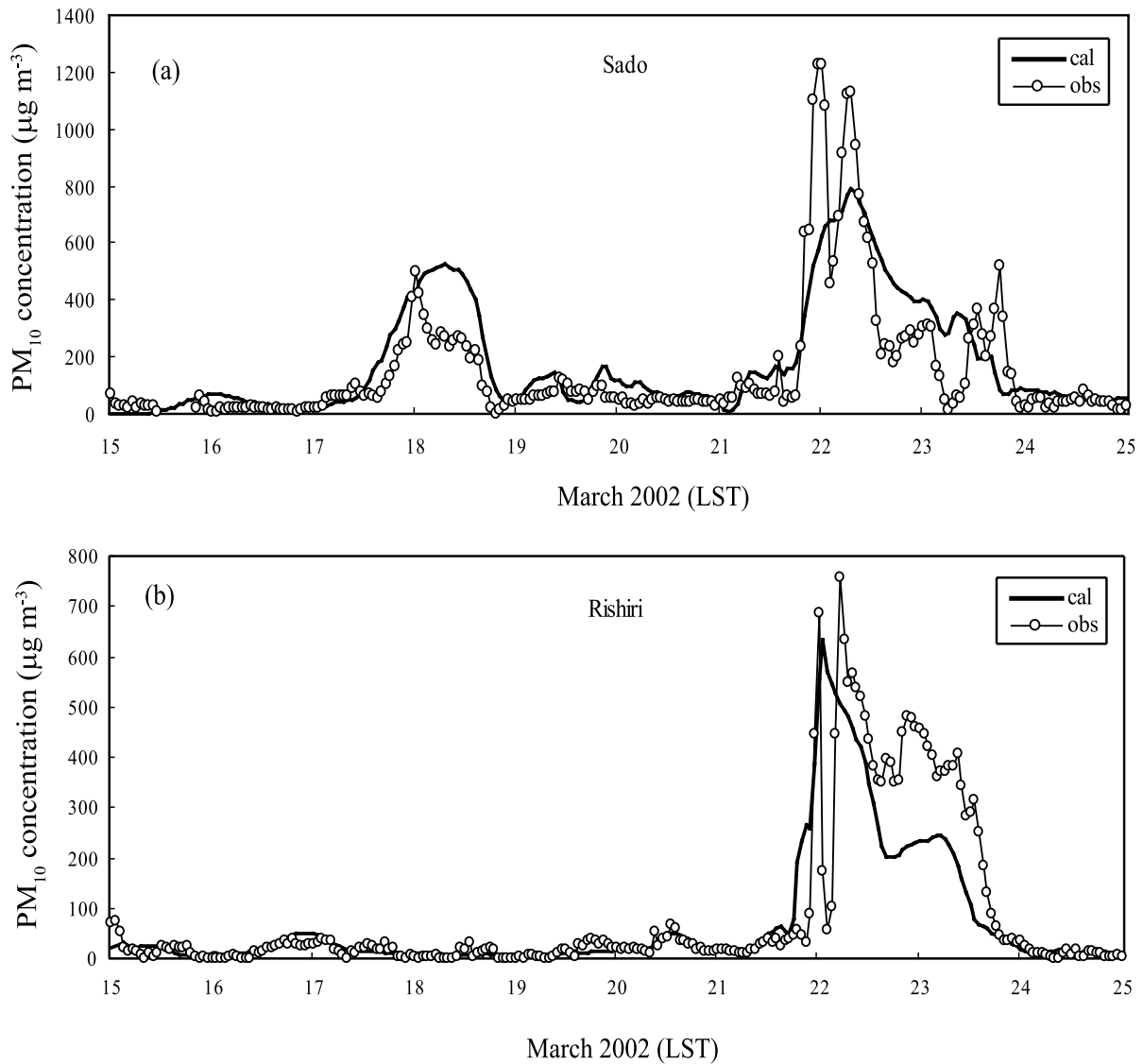
Figure 9. The time series of simulated and observed hourly PM_{10} concentrations for the period of 15–24 March 2002 (LST) at (a) Sado and (b) Rishiri (unit: $\mu g\ m^{-3}$).

cesses for fine particles and consequently, fine particles are favorable to be transported over longer distance to apparently change the particle levels downwind. During dust storm periods, dust particle mass loadings are extremely high in almost all size ranges. During nondust periods, although sea-salt aerosol is an important contributor to total mass loading of particles in coastal regions, it has lower mass loading in fine mode (<2 μm).
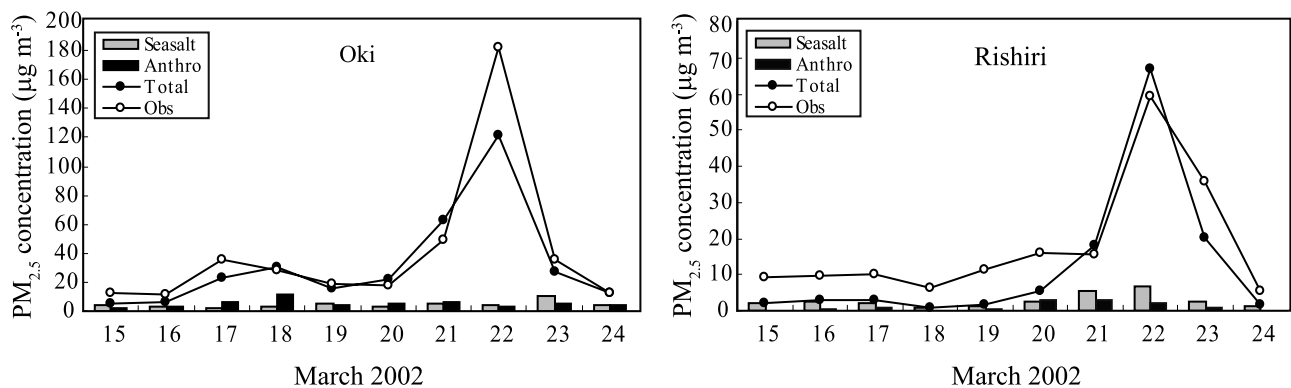
Figure 10. Simulated and observed daily average $PM_{2.5}$ concentrations (unit: $\mu g\ m^{-3}$) at two remote sites in Japan.
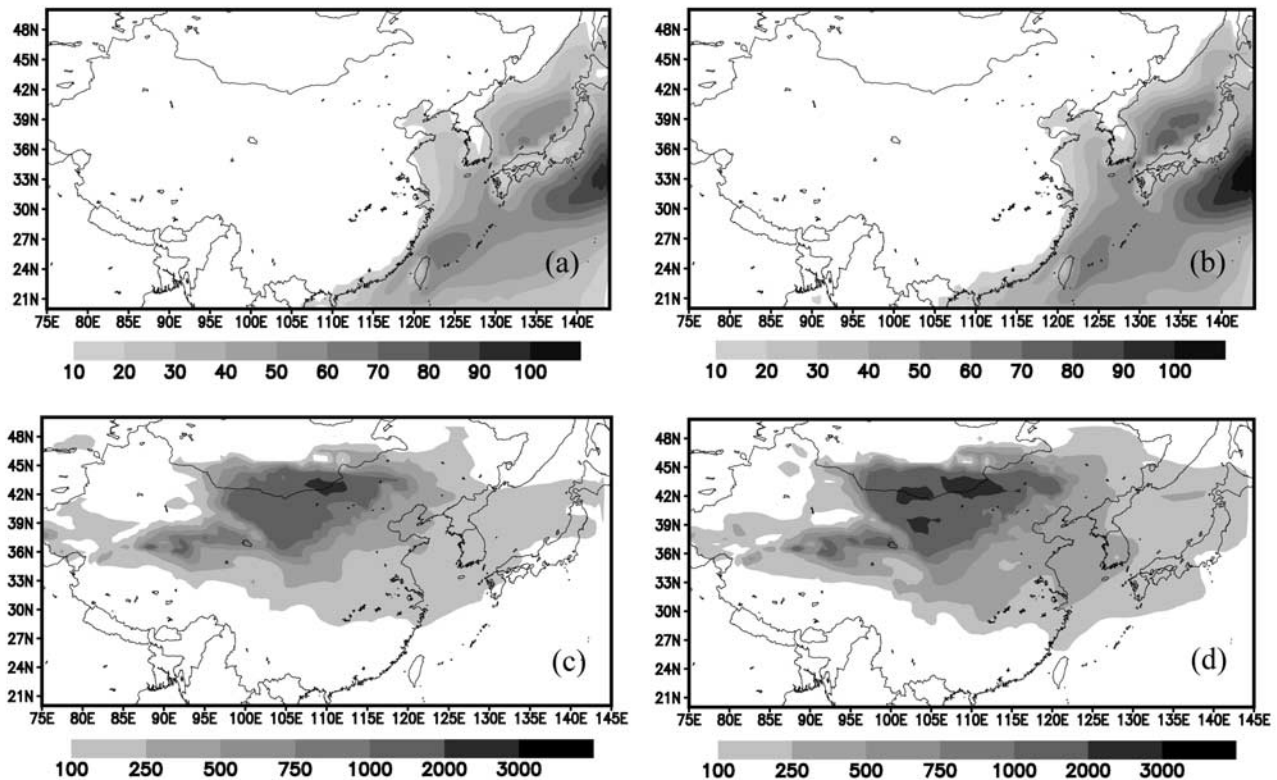
Figure 11. Average surface sea salt concentrations ($\mu g\ m^{-3}$) for the period of (a) 15–24 March and (b) 19–23 March, and average surface dust concentrations ($\mu g\ m^{-3}$) for the period of (c) 15–24 March and (d) 19–23 March 2002. See color version of this figure at back of this issue.

Therefore anthropogenic sources show an evident effect on downwind fine particles in nondust days. The discrepancy between simulation and observation for nondust periods may be attributed to the following factors: (1) underestimation of anthropogenic particulate emission in the emission inventory, and (2) inaccuracy in particle mass size distribution of anthropogenic emission, which determines the size spectrum of airborne particles and consequently dominates their residence time in the air. (3) Secondary aerosols formed by gas-particle interaction may enhance the magnitude of particle mass loading to some extent.

4.4. Distribution of Sea-Salt and Dust Mass Concentrations

[27] Figure 11 shows the averaged sea-salt and dust particle concentrations over entire study period (10 days from 15 to 24 March 2002, Figures 11a and 11c) and over the second dust storm period (5 days from 19 to 23 March 2002, Figures 11b and 11d). Three high concentration centers of sea-salt aerosols (Figure 11a) are located over the East China Sea, the Sea of Japan and the western Pacific Ocean southeast of Japan, with average concentrations of 60–70, 50–60 and 80–90 $\mu g\ m^{-3}$, respectively. Sea-salt concentrations have been apparently enhanced during the second dust storm period (Figure 11b), especially over the Sea of Japan and ocean southeast of Japan, with average concentration up to 80 and 100 $\mu g\ m^{-3}$, respectively. Sea-salt aerosols show considerable levels over Japan with 10-day averaged concentrations of 20–30 $\mu g\ m^{-3}$

over most of Japan and up to 40 $\mu g\ m^{-3}$ in coastal areas (Figure 11a).

[28] The highest dust concentration occurs in the Gobi desert of southern Mongolia and northern Inner-Mongolia, with a maximum of 10-day averaged value being 3000 $\mu g\ m^{-3}$ along the southeastern China-Mongolia border (Figure 11c). Another high dust load region lies from Kumtag to Badain Juran desert, with a center of 1000–2000 $\mu g\ m^{-3}$ at the Kumtag desert. Dust level is relatively low (100–250 $\mu g\ m^{-3}$) in the Taklimakan desert during this period. In Figure 11d the areas with highest dust concentrations are enlarged along the southern China-Mongolia border, associated with the strong dust deflations during the second dust storm. Northern China, especially Inner Mongolia, experience very high soil dust level as well due to its location of or proximity to source regions. During the second dust storm period, portions of Tulufan and Zhunge'er basin experience the elevation of soil dust, with 5-day averages being 100–250 $\mu g\ m^{-3}$. The dust outflow from the Asian continent to the western Pacific Ocean is clearly illustrated in Figures 11c and 11d. Remarkable influence of mineral dust is found to reach the Yangtze River (including Yangtze Delta), the China Yellow Sea, the Korean peninsula, and the western coast of Japan, with the averages of 100–250 $\mu g\ m^{-3}$ for 10 days (Figure 11c). For the second dust storm (Figure 11d), considerable influence of soil dust with average dust concentrations of 100–250 $\mu g\ m^{-3}$ extends to portions of southeastern China and almost all of Japan. Dust levels are enhanced up to 250–500 $\mu g\ m^{-3}$ over South Korea, the China Yellow Sea, as well as the northern Yangtze Delta. Dust concentrations of
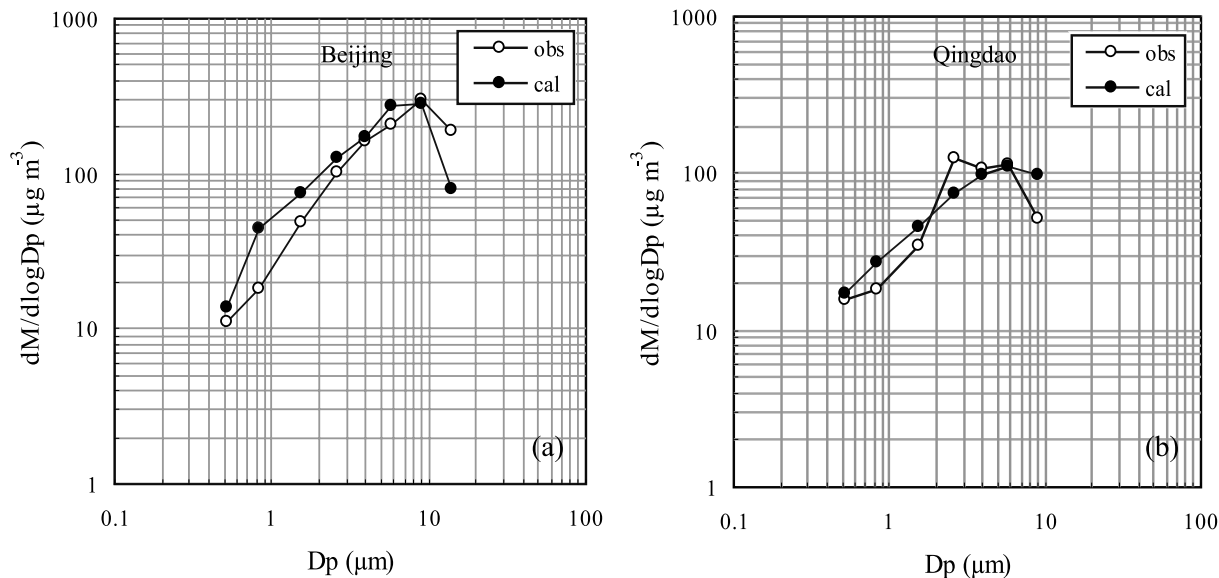
Figure 12. Comparison between simulated and observed size-segregated particle concentrations at (a) Beijing (averaged from 1000LST 19 March to 1000LST 21 March 2002) and (b) Qingdao (averaged from 1000LST 20 March to 1000LST 23 March 2002).

$500-750$ μg m^{-3} appear in the vicinity of Beijing and portions of northeast China.

4.5. Validation and Analysis of Particle Mass Size Distribution

[29] Figure 12a shows the modeled and observed particle concentrations of eight size bins at Beijing, averaged over 2 days from 1000 LST 19 March to 1000 LST 21 March 2002. The arrival time of the dust storm at Beijing is around 0800 LST 20 March, and it lasts more than 24 hours. Both observation and simulation clearly show a mono-peak at a coarse size range $7-11$ μm. Model simulation agrees with observation quite well except for the size bin >11 μm and $0.65-1.1$ μm. *Mori et al.* [2003] measured mass size distribution of aerosol at Beijing during a dust storm originating from the southern Mongolia desert on $21-24$ March 2001. A mono-peak was found at $4.7-7.0$ μm. It is worthwhile to note that the size range with peak mass loading shifts to a coarser mode ($7.0-11.0$ μm) associated with the increasing intensity of the dust storm on 20 March 2002. Figure 12b presents the simulated and observed particle spectral mass concentrations at Qingdao site, averaged from 1000 LST 20 March to 1000 LST 23 March 2002. The arrival time of dust at Qingdao is around 2100 LST 20 March. Noticeably, a bimodal shape occurs in observation. Modeled particle mass concentrations are consistent with observations in most of the size bins, and the model accurately captures the peak in the size range $4.7-7.0$ μm. However, the model fails to reproduce another peak at $2.1-3.3$ μm. It is of much interest to explore this phenomenon in detail. Although a part of the aerosol sample at Qingdao is collected in nondust periods, locally produced particles from anthropogenic origin seem incapable of causing this peak because of their much smaller proportion compared with dust aerosols. Analysis of sampling data

collected during a nondust period (between 1130 LST 8 March and 1130 LST 14 March 2002) at the same site clearly reveals that an averaged maximum of 15.5 μg m^{-3} appears in a fine mode ($0.65-1.1$ μm), and the average TSP concentration was about 77.3 μg m^{-3} for this period, indicating the magnitude and size distribution pattern of particles resulting from anthropogenic origin. Secondarily formed particles through heterogeneous gas-particle interaction are also not supposed to be the major contributor to this peak because of the weak interaction in the relatively dry continental atmosphere during the outbreak of the dust storm [*D. Zhang et al.*, 2003]. Thus it is supposed that the supplementation of particles along the transport pathway or from other dust source origins may be responsible for this peak.

[30] Figure 13 shows the backward trajectories started from Beijing and Qingdao during the second dust storm. The trajectories are calculated on line with HYSPLIT model of NOAA Air Resources Laboratory (http://www.arl.noaa.gov/ready/hysplit4.html). The backward trajectories are initiated every 3 hours with the starting point at 1000 m and 200 m elevations over both Beijing and Qingdao and followed by 24 hours except for the trajectories from 200 m over Qingdao, which are calculated for 48 hours. The backward trajectory calculations are from 1600 UTC 20 March to 1900 UTC 21 March for Qingdao and from 0100 UTC to 2200 UTC 20 March for Beijing. For trajectories started from 1000 m, similar patterns are shown with prevailing northwesterly flow to both Beijing and Qingdao (Figures 13b and 13d), indicating the major transport pathway in upper layers. However, large differences exist in the trajectories starting from 200 m. The trajectories from Beijing are still northwesterly (Figure 13a), but those started from Qingdao show more complex pathways (Figure 13c). Some air parcels originating from the Gobi desert are directly transported to Qingdao by north-
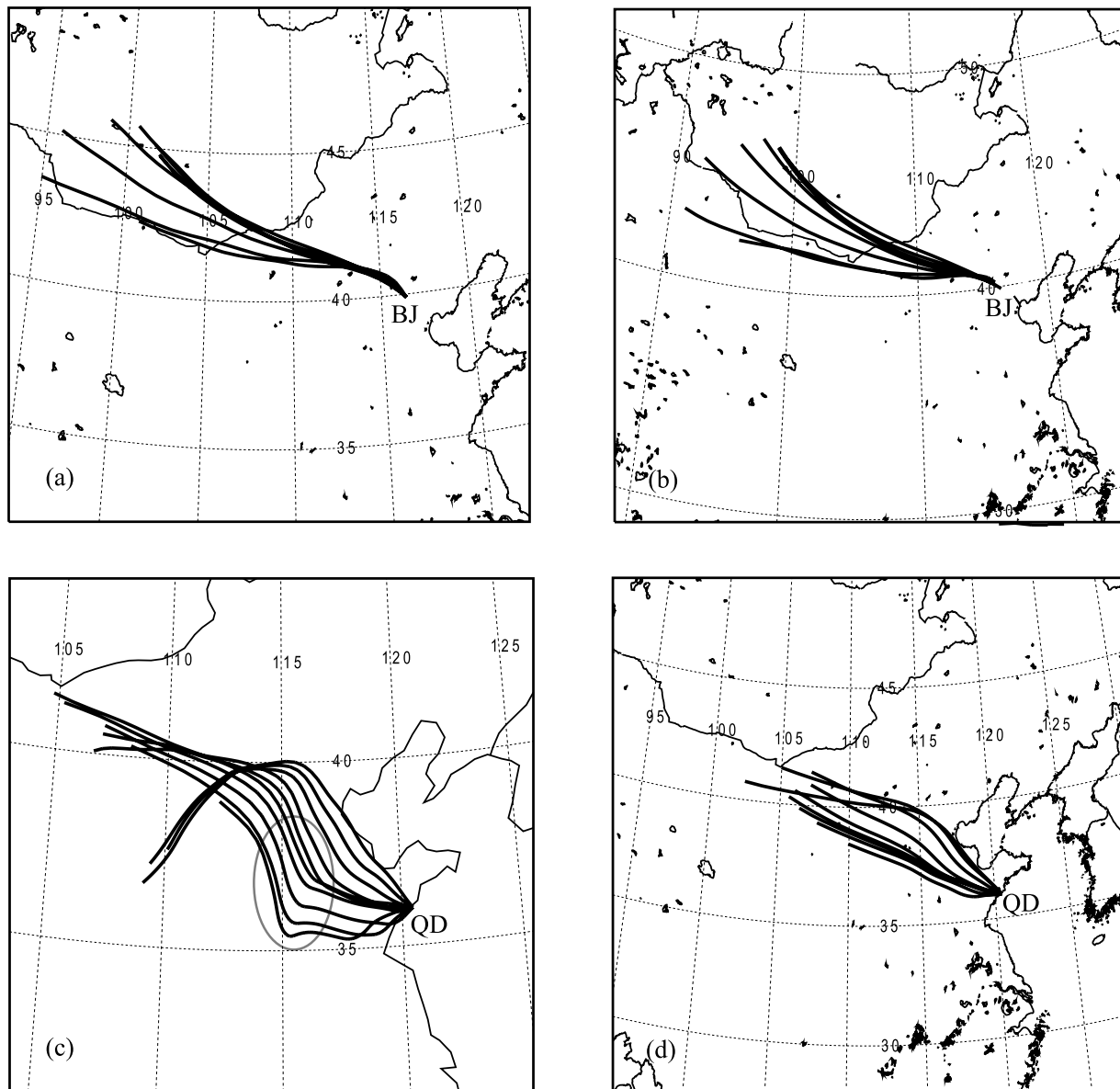
Figure 13. Backward trajectory calculations initiated every 3 hours with the starting point of (a) 200 m over Beijing, (b) 1000 m over Beijing, (c) 200 m over Qingdao, and (d) 1000 m over Qingdao. Trajectory calculations are from 0100UTC to 2200UTC 20 March 2002 for Beijing and from 1600UTC 20 March to 1900UTC 21 March 2002 for Qingdao. Duration of the calculation is 24 hours for Figures 13a, 13b, and 13d and 48 hours for Figure 13c.

westerlies, while quite a few air parcels first move southeastward from desert regions, and then move nearly southward along 115°E longitude, followed by turning around and moving eastward to Qingdao. These air parcels pass over portions of Shanxi, Shangdong and Henan Provinces where considerable semiarid lands still exist (elliptical circle in Figure 13c) and likely have a different soil texture and size distribution of dust emission from that in the Gobi desert. Uplifted soil dusts from those regions may refill the original dust plume and change its property in particle size distribution and consequently create another observed peak at 2.1–3.3 μm at Qingdao. Noticeably, there are actually some dust-rise reports in above discussed areas on 21 March (Figure 3d), which support the above analysis.

The regions mentioned above are categorized as cropland in this study and are usually neglected in present land use maps. Moreover, soil texture and size spectrum of dust emission in those regions is still absent now due to the lack of measurements. This suggests the importance of land use and soil property information in model simulation.

[31] During the second dust storm, particle number concentrations observed in Nagasaki University showed a significant increase of particles in almost all size ranges [*Arao and Ishizaka*, 2002]. Figure 14 shows the simulated particle mass size distribution averaged from 1200 LST 21 March to 0900 LST 22 March 2002 and that converted from observed particle number concentrations at Nagasaki by assuming a spherical shape of particles with a constant
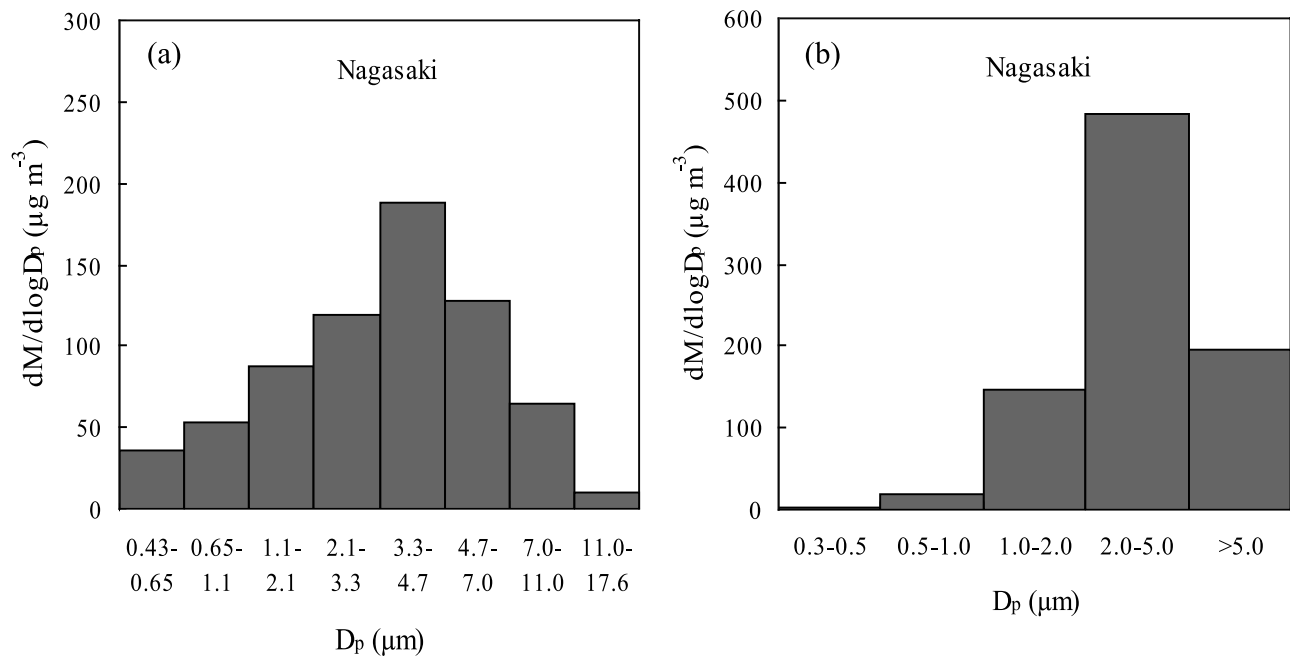
Figure 14. Particle mass size distribution at Nagasaki, averaged from 1200LST 21 March to 0900LST 22 March 2002. (a) Simulated concentrations and (b) values converted from observed number size distributions by OPC assuming a constant particle density of 2.6 g cm^{-3}.

density of 2.6g cm^{-3}. The converted average total mass concentration of 856 μg m^{-3} is very close to the value of 796 μg m^{-3} measured simultaneously by a high volume sampler. The differences may be due to the improper selection of constant particle density (2.6g cm^{-3}) because sea-salt and other kinds of aerosols may be mixed with soil dust and lower the chosen particle density. Although an exact comparison is not available because of the slightly different size ranges used in OPC, a similar pattern in mass size distribution between observation and simulation can be clearly seen from Figure 14. The simulated size range, which accommodates peak mass concentration, is at 3.3–4.7 μm (Figure 14a), falling into the observed size range 2.0–5.0 μm in which a peak of 486 μg m^{-3} is accommodated (Figure 14b). The simulated particle mass concentrations in the size ranges 1.1–2.1 μm, 2.1–4.7 μm, and >4.7 μm are about 98, 307, and 202 μg m^{-3}, respectively, reasonably consistent with the observed values of 145, 482, and 194 μg m^{-3} in the size ranges 1.0–2.0 μm, 2.0–5.0, and >5.0 μm.

[32] Figure 15 presents the daily average particle mass size spectrum at Shanghai, China, and western coastal sites of Japan on 22 March when the second dust storm prevails. An apparent feature appears that the size range with maximum mass loading tends to shift to finer mode along the pathway from source regions to downwind areas, with a mono-peak in the size range 3.3–4.7 μm at Shanghai, 4.7–7.0 μm at Oki and Sado-seki, and 3.3–4.7 μm at Rishiri. These results are consistent with recent findings [*Mori et al.*, 2003; *In and Park* 2003; *Duce*, 1995]. Figure 15 shows that the peak mass loading of sea-salt aerosols generally settles in the size range 4.7–7.0 μm at the western coast of Japan. This result is consistent with previous work of *Gong et al.* [1997a, 1997b] in which the size range around 6 μm

(in diameter) was found for peak mass loading of sea-salt aerosols.

[33] The above validation shows a general agreement between simulation and observation in particle mass size distribution, indicating the model's capability in studying the major features of particle size-segregation. Different size distribution patterns of soil dust at locations along the transport pathway are determined by a series of complex factors including size spectrum of vertical dust flux in source regions, highly varied dry deposition velocity among size bins over different land use types, size-dependent wet removal rates, as well as the property of entrained soil dust along the transport pathways.

5. Particle Deposition and Budget

5.1. Dry Deposition Velocity and Deposition of Soil Dust Particles

[34] Figures 16a and 16b show the simulated dry deposition velocity (V_d) for particles with a size of 0.84 μm and 4 μm in diameter, averaged over 5 days from 19 to 23 March 2002. In Figure 16a, 5-day averaged friction velocity is also shown (in contour). There are several high u_* zones in the domain, such as the southeastern China-Mongolia border and the western Pacific Ocean southeast of Japan, resulting from high wind speed. u_* is large near the China-North Korea border and in western parts of Japan due to strong wind shear in the mountains. The interactions of continental outflow with southwesterly flow resulting from a high-pressure system over the western Pacific Ocean south of Japan also enhance the friction velocity along the western coast of Japan. High u_* zones along the northern fringe of the Tibet Plateau are partly due to steep topography. For particles with a size of 0.84 μm, V_d shows a high
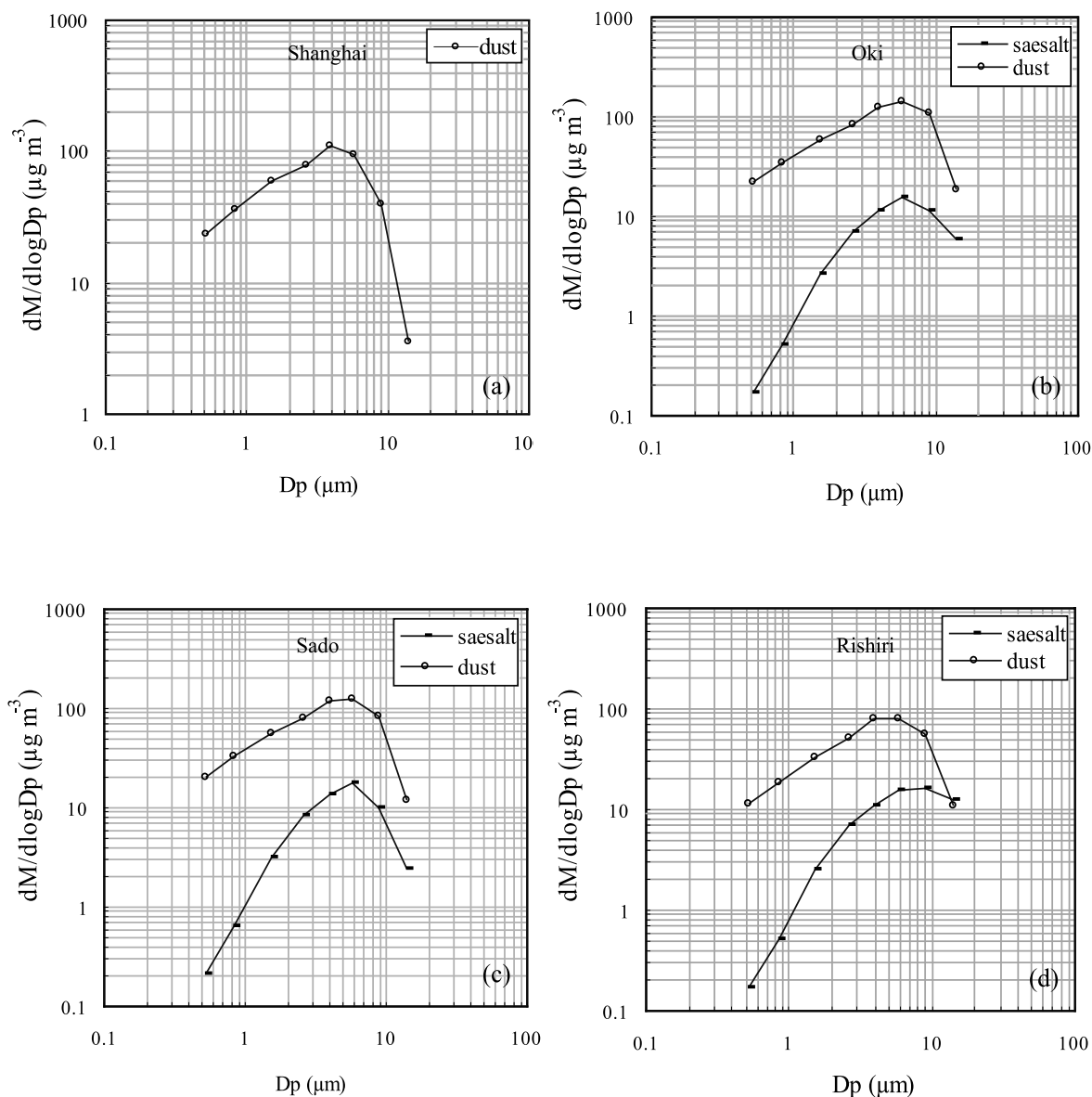
Figure 15. Daily averaged particle mass size distribution at (a) Shanghai, (b) Oki, (c) Sado, and (d) Rishiri on 22 March 2002.

variability within the domain, ranging from 0.01 to 0.2 cm s^{-1} on average (for particles with a density of 2.6 g cm^{-3}). Neither Brownian diffusion nor impaction and interception are effective for particles with this size; u_* becomes more important in determining V_d. Higher V_d values occur over the southeastern China-Mongolia border, the China-North Korea border, and the western coast of Japan, as well as the northern fringe of the Tibet Plateau. Relatively lower V_d values are found over water surfaces and portions of the northwestern desert regions. For coarser particles with a size of 4 μm, impaction and interception become more effective. Besides the consistency with u_*, V_d also shows a remarkable enhancement over vegetated areas, such as western portions of northeast China, the northern China-North Korea border, the western coast of Japan, as

well as the western part of Sichuan province of China. Higher V_d over the ocean southeast of Japan Island is a result of the influence of disturbed water by strong wind there. Modeled size-segregated V_d values agree reasonably with previous field observations and studies [*Giorgi*, 1986; *Zhang et al.*, 2001].

[35] The total dry deposition of soil dust is calculated by the sum of flux for each size bin. Figures 16c and 16d show the distributions of dry deposition of soil dust (unit: g m^{-2}) integrated over 10 days and 5 days. Maximum dry deposition up to 30 g m^{-2} for 10 days occurs in the Gobi desert along the southeastern China-Mongolia border. High dry deposition of 10–20 g m^{-2} covers wide desert areas of southern Mongolia and northern Inner-Mongolia. It is worthwhile to note that a high dust deposition zone lies along the northern
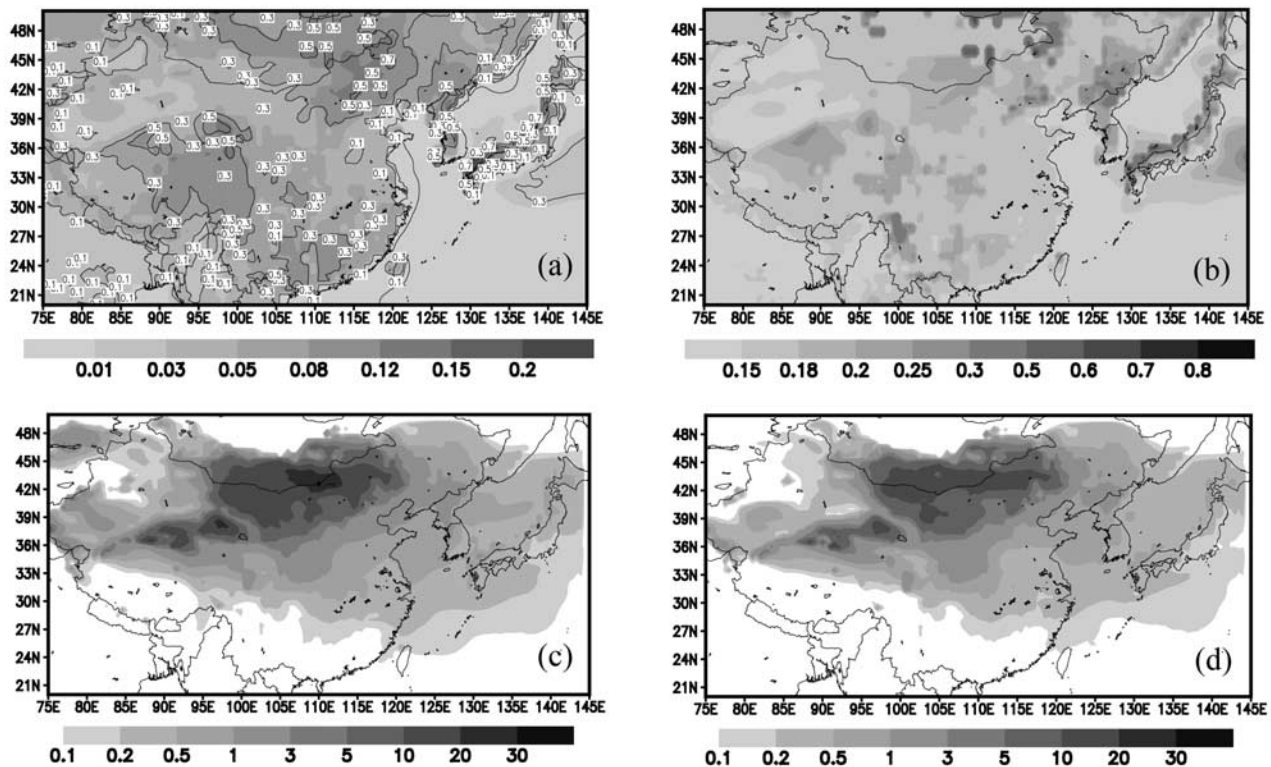
Figure 16. Spatial distribution of averages of (a) friction velocity (m s^{-1}) and particle Vd (cm s^{-1}) for a size of 0.84 μm, (b) Vd (cm s^{-1}) for a size of 4 μm, (c) total dry deposition (g m^{-2}) for the period of 15–24 March, and (d) total dry deposition (g m^{-2}) for the period of 19–23 March 2002. See color version of this figure at back of this issue.

fringe of the Tibet Plateau, with a maximum of 20–30 g m^{-2} located between the Kumtag and Badain Juran desert. The formation of this band is mostly attributed to the larger V$_d$ around steep topography (Figures 16a and 16b) and the higher percentage of coarse particles in the Chinese western desert. Total dry deposition as high as 3 g m^{-2} is found over most parts of northern and western China and the Korean peninsula (Figure 16c). Dry deposition in this study can be comparable with the results of *Zhao et al.* [2003] in which a spatial pattern of cumulative dry deposition of soil dust with the size range <41 μm was derived for spring 2001. Our results also have the same order as the results of *Zhang et al.* [1998] in which an average flux of 50 g m^{-2} mon^{-1} was derived over the Chinese Northern Desert for spring 1994. Dry deposition shows a close correlation with the spatial distribution of dust concentration shown in Figures 11c and 11d. The magnitude of dry deposition along the western coast of Japan is in the same range (0.5–1.0 g m^{-2}) as that over the China Yellow Sea and western parts of the Korean peninsula (Figures 16c and 16d) due to larger V$_d$ in those regions (Figures 16a and 16b). This indicates that dry deposition is determined by both dust concentration and dry deposition velocity (V$_d$), which is highly varied among different land use categories, particle size bins, as well as meteorological conditions.

5.2. Scavenging Rate and Wet Deposition of Soil Dust Particles

[36] There are few detailed investigations on wet deposition in previous studies of Asian dust. Some of the studies include wet deposition process by assuming the scavenge rate just dependent of precipitation rate and independent of particle size. However, scavenging rate in fact has a significant dependence on particle size. Some of the previous works and measurements [*Andronache*, 2003; *Seinfeld and Pandis*, 1998] revealed the importance of below cloud scavenging for very small particles (<0.01 μm) and coarse particles (>2 μm, such as dust and sea-salt aerosols), and the unimportance for particles in accumulation mode. It is therefore necessary to realistically represent these features in aerosol model, especially in the study of size-segregated airborne particles and depositions. Figure 17a presents the comparison between simulated and observed total precipitation at four EANET sites and three WMO surface weather stations in southern China, Nanchang (NC, 115.91°E, 28.6°N), Fuzhou (FZ, 119.27°E, 26.08°N), and Shaoguan (SG, 113.57°E, 24.8°N). Precipitation predicted by MM5 appears to be in a reasonably good agreement with observation, with better performance at Sado-seki, and a relatively poor result at Hedo site. The model tends to underpredict observation by a factor of 3 at Hedo site, probably due to stronger convective activities over those ocean areas, which are usually difficult to predict with current meteorological models. Figure 17b shows the simulated pattern of total precipitation from 15 to 24 March 2002. Precipitation is scarce over most of dust source regions and appears along the Shandong peninsula, China Bohai bay and portions of northeastern China which are also characterized by major export zones of continental dust. An apparent rain belt occurs, extending from south-
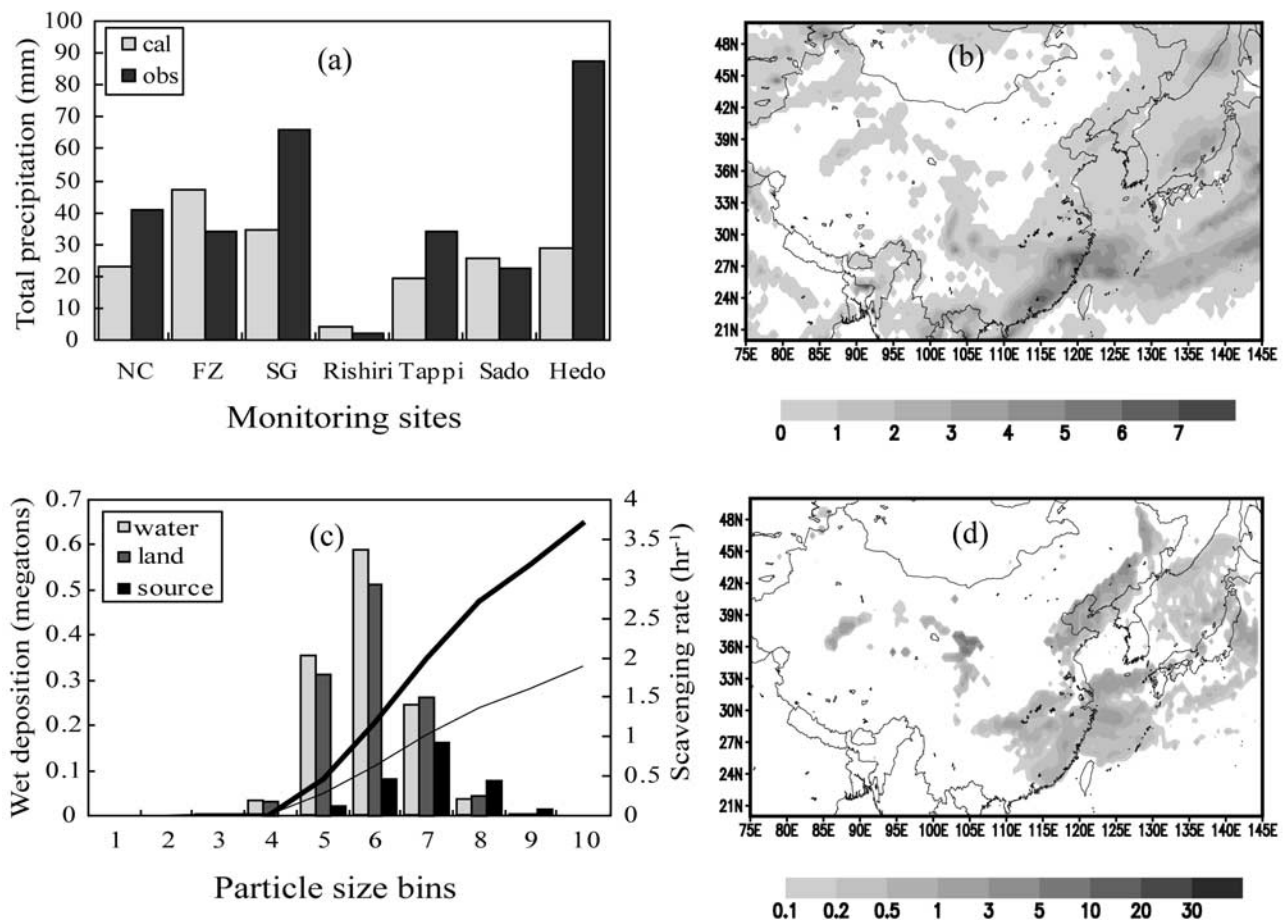
Figure 17. (a) Simulated and observed total precipitation (mm) at seven monitoring sites, (b) simulated distribution of total precipitation in the domain (cm), (c) bin resolved dust wet deposition (megatons) (for three kinds of underlying surfaces) and scavenging rate (hour^{-1}) under the precipitation rate of 1 mm h^{-1} (thin line) and 3 mm h^{-1} (thick line), and (d) total wet deposition of soil dust (g m^{-2}) in the domain for the period of 15–24 March 2002. See color version of this figure at back of this issue.

eastern China, and passing across the East China Sea to the western Pacific Ocean southeast of Japan, with maximum precipitation amount reaching 70 mm for 10 days.

[37] Figures 17c and 17d show the bin resolved wet deposition over three representative underlying surfaces (dust source region, land other than source region and water) and total wet deposition of soil dust on 15–24 March 2002. Figure 17c also shows the particle scavenge rate (R) for each size bin under low (1 mm h^{-1}) and moderate (3 mm h^{-1}) precipitation rate. It is clear that R varies substantially among all size bins, with much lower scavenging rate for fine particles (0.43–2.1 μm, first 3 size bins in Figure 17c) and higher one for larger particles (>2.1 μm), increasing with particle size. Scavenging rate also strongly depends on precipitation, showing an increase by about a factor of 2 when precipitation rate varies from 1 mm h^{-1} to 3 mm h^{-1}. Modeled scavenging rates are consistent with the recent findings of *Andronache* [2003] in which the below-cloud removal of particle was studied by using an explicit calculation method and field experiments in various environments. Figure 17c shows that the wet deposition is much lower for the first 3 size bins over all three types of underlying surfaces, due to the smallest scavenge rate for these size ranges. Over land and water

surface, wet deposition shows maximum in the size range 4.7–7.0 μm (6th size bin) and second maximum in 3.3–4.7 μm (5th size bin) as a result of a combined contribution from size-defined scavenging rate and mass loading, whereas for source regions, wet deposition is much lower and shows maximum in size range 7.0–11.0 μm.

[38] Total wet deposition is estimated by summing up wet deposition flux for each size bin. Wet deposition shows a general consistence with precipitation pattern, with higher values over southeastern China, the East China Sea, the Sea of Japan, as well as the export zones mentioned above (Figure 17d). Although the precipitation is relatively low (<2 cm) over the export zones, wet deposition is found comparable to other regions, such as the Sea of Japan and the East China Sea, due to high dust mass loading and larger scavenge rate for coarser particles. Compared with dry deposition (Figure 16c), wet deposition is much smaller over most of the continent. Noticeably, wet deposition appears to be comparable with dry deposition over the export zones of northeast China and the Sea of Japan, and exceeds dry deposition over southeastern China, the East China Sea and portions of the Pacific Ocean east of Japan. These results indicate the important role of the wet deposition process in removing dust particles, even in springtime

Table 2. Dust Budget for Typical Regions in the Domain on 15–24 March 2002[a]

Region	Emission	Dry Deposition	Wet Deposition
Source region 1	20.74	10.77	0.07
Source region 2	10.37	5.32	0.02
Source region 3	12.08	8.15	0.26
Land other than source region	0.0	4.98	1.18
Ocean or sea	0.0	1.30	1.26

[a]Units are in megatons.

dust storm periods when precipitation is relatively low or moderate. The above results also reveal that while dry deposition dominates total deposition near source regions, wet removal plays a more important role in the intermediate pathway of dust transport and downwind of source regions during dust periods.

5.3. Dust Budget Estimation and Analysis

[39] Dust budget estimation including dust emission, dry and wet depositions for different regions on 15–24 March 2002 is listed in Table 2. The three source regions in Table 2 represent three categories of major dust sources shown in Figure 1. Total dust emission for three categories of source regions for the period of 15–24 March 2002 is estimated to be 43.2 megatons. About 71% of total emission (30.5 megatons) is redeposited onto ground surface through dry deposition process, with 56% of total onto source regions, 12% onto other land categories and 3% onto ocean or sea. Wet deposition accounts for 6% (2.8 megatons) of total mass emitted, with 1.26 megatons onto water surface. The remaining 23% (9.9 megaton) of total emitted particles is suspended in the atmosphere or subject to long-range transport.

[40] In the study of *Zhao et al.* [2003], averaged dust emission over major source regions was estimated to be 5.36 tons km^{-2} for March 2001, and approximately 55% of total emitted dust particles was redeposited onto major source regions. In this study, averaged dust emission over the three source regions is about 9.02 tons km^{-2}, with 56% redeposited onto source regions. Considering the dust storm in this study to be the most severe one in the past decade, our estimation appears to be reasonably consistent with the result of *Zhao et al.* [2003]. Net export of dust particles from three source regions to atmosphere is about 18.6 megatons in this study, which can be comparable to the estimation of *Shao et al.* [2003] for the period of 15 to 24 March, 2002. Land surfaces other than source regions including most parts of East China, the Korean peninsula and Japan show a pure sink of soil dust, receiving totally 6.16 megatons of dust particles by dry and wet deposition which accounts for 4.98 and 1.18 megatons, respectively. Dry deposition decreases from source regions to ocean and sea. In contrast, wet deposition is increasing on the transport pathway of the dust storm.

6. Summary and Conclusions

[41] Dust events on 15–24 March 2002 have been investigated by using an aerosol model, which is coupled with a Regional Air Quality Model driven by MM5. The focuses of this study have been placed on the validation and analysis of size-segregated features of soil dust particles including the spatial and temporal variability of particles in various size ranges, size-segregated dry deposition and wet deposition, as well as dust mass budget. Various observational data including WMO surface weather observations, near-surface concentrations of PM$_{10}$ and PM$_{2.5}$, particle size distribution measured by Andersen sampler and OPC over and downwind of the source regions, have been used to evaluate the model performance and model capacity. An agreement has been obtained between simulation and observation in terms of evolutionary pattern of the dust storm. The starting and ending times of the dust storm are accurately predicted by the model. The validation indicates the model's capacity in capturing most of major features of particle size segregation and reasonably reproducing particle mass loadings in various size ranges (including PM$_{10}$, PM$_{2.5}$, and mass loadings in other size ranges) along the dust transport pathway. The above validation supports the reliability of this numerical study and brings us some confidence in carrying out subsequent analysis and estimation.

[42] Peak mass loading and its accommodated size range are reasonably reproduced at Beijing and Nagasaki, where a mono-modal shape is found in particle mass size distribution. A bimodal shape appears at the Qingdao site, mainly resulting from the additional mixture of soil dust from semiarid areas along the transport pathway of the dust storm. The model simulation misses the peak at 2.1–3.3 μm, mainly due to the limited information on soil properties in semiarid areas on the intermediate transport pathway to Qingdao. A remarkable tendency has been both simulated and observed, showing a shift of size range with peak mass load from coarse mode to finer mode on the pathway from source origins to distant downwind areas.

[43] Sea-salt aerosols are found to have a considerable influence on airborne particles over Japan, with 10-day averages of 20–30 μg m^{-3} over most of Japan and up to 40 μg m^{-3} in coastal areas. The major deflation regions are southern Mongolia, northern and western Inner Mongolia, the southern and southeastern China-Mongolia border, as well as portions of western China, such as the Kumtag desert. Dust emission is relatively small in the Taklimakan desert for this period. Ten-day averaged total dust mass loading as high as 3000 μg m^{-3} occurs in the Gobi desert along the southeastern China-Mongolia border. The Yangtze River of China, The China Yellow Sea, the Korean peninsula, as well as the western coast of Japan experience an average concentration of 100–250 μg m^{-3} for the 10-day period. The influence of the second dust storm reaches portions of southeastern China and almost all of Japan, with 5-day averaged concentration being 100–250 μg m^{-3}. Dust concentrations are enhanced up to 250–500 μg m^{-3} over South Korea, the China Yellow Sea and the northern portion of the Yangtze Delta, and reach 500–750 μg m^{-3} in the vicinity of Beijing and portions of northeast China.

[44] V$_d$ shows its high variability among various underlying surfaces, meteorological conditions, and particle size ranges. For particles with a size of 0.84 μm, V$_d$ shows a close relationship with u$_*$ due to their less dependence on Brownian diffusion, impaction and interception. For coarser particles with a size of 4 μm, impaction and interception

become more effective. V_d shows a remarkable enhancement over vegetated surface over western portions of northeast China, the northern China-North Korea border, the western coast of Japan, as well as the western portion of the Sichuan province of China. Scavenging rate varies largely among size bins, and depends on precipitation. Wet removal shows high scavenging efficiency for coarser particles (>2 um) and trivialness for particles in the accumulation mode.

[45] Large dry deposition occurs in source regions of southern Mongolia and northern Inner-Mongolia, the northern fringe of the Tibet Plateau, the Korean peninsula, as well as the western coast of Japan. Maximum dry deposition up to 30 g m^{-2} for 10 days is found in the Gobi desert along the southern China-Mongolia border. Budget analysis indicates that total dust emission of 43.2 megatons is emitted into the atmosphere during the 10-day period. About 71% (30.2 megatons) of total mass is redeposited onto the underlying surface, with 56% of the total onto the source regions. Wet deposition accounts for 6% of total emitted dust particles. The distribution and magnitude of particle deposition are strongly dependent on both concentration and size-segregated V_d and scavenging rate. While dry deposition dominates the removal of particles over source regions, the influence of wet deposition is increasing along the transport pathway of the dust storm. Over the export zones of northeast China, the Sea of Japan, southeastern China and the East China Sea, as well as the ocean southeast of Japan, wet deposition is found to be comparable or exceed dry deposition.

[46] Compared with previous numerical studies on Asian dust, this work focuses on model prediction and analysis of particle size segregation, size-defined dry and wet depositions, as well as dust mass budget, by using a developed aerosol model which includes a land use map based on NDVI retrieved database, a dust emission model parameterized by friction velocity, near-surface relative humidity and vegetation cover, and physically sound schemes for dry and wet deposition processes. Combined with a transport model and MM5, this model system has achieved satisfactory results that exceed our expectation. Model results are not only in an agreement with observations but are also reasonably consistent with related previous works. The usage of up-to-date size distributions of vertical dust flux, reasonable parameters for dust deflation, and physically explicit parameterizations of dry and wet deposition processes in the aerosol model favors the model performance in this study. Given such a validation result, particle size segregation, depositions and budget are further investigated. Land use and soil texture information are found to be important in the prediction of dust emission and airborne dust particles. Some deficiencies in the model simulation are probably just associated with the limitation in the present knowledge of land use and soil property, such as underestimation of dust emission in parts of the Chinese western desert, lower hourly peak concentration in downwind regions, as well as the missing peak at Qingdao. It could be expected that the application of a more detailed land use database and simulation with a higher model resolution will further improve the model performance. Further investigation of land use characteristics and devel-

opment of the aerosol model, especially in the physically explicit dust emission scheme and the gas-particle interaction mechanism, are recommended and planned to continue the study of these issues in the future.

References

An, J., H. Ueda, K. Matsuda, H. Hasome, and M. Iwata (2003), Simulated impacts of SO$_2$ emissions from the Miyake volcano on concentration and deposition of sulfur oxides in September and October of 2000, *Atmos. Environ.*, *37*, 3039–3046.

Andronache, C. (2003), Estimated variability of below-cloud aerosol removal by rainfall for observed aerosol size distributions, *Atmos. Chem. Phys.*, *3*, 131–143.

Arao, K., and J. Ishizaka (2002), Yellow sand dust events observed at Nagasaki region in 2002 and a preliminary observation of aerosols on the sea and a mountaintop, *Atmos. Environ. Impacts Aerosols East Asia Res. Rep.*, 19–20.

Brasseur, G. P., J. J. Orlando, and G. S. Tyndall (1999), *Atmospheric Chemistry and Global Change*, pp. 349–366, Oxford Univ. Press, New York.

Byun, D. W., and R. Dennis (1995), Design artifacts in Eulerian air quality model: Evaluation of the effects of layer thickness and vertical profile correction on surface ozone concentrations, *Atmos. Environ.*, *29*, 105–126.

Carmichael, G. R., L. K. Peters, and T. Kitada (1986), A second-generation model for regional-scale transport/chemistry/deposition, *Atmos. Environ.*, *20*, 173–188.

Chamberlian, A. C. (1983), Deposition and resuspension, in *Precipitation Scavenging, Dry Deposition, and Resuspension*, edited by H. R. Pruppacher, R. G. Semonin, and W. G. N. Slinn, pp. 731–751, Elsevier Sci., New York.

Charlson, R. J., J. E. Lovelock, M. O. Andreae, and S. G. Warren (1987), Oceanic phytonplankton, atmospheric sulphur, cloud albedo and climate, *Nature*, *326*, 655–661.

DeFries, R. S., and J. R. G. Townshend (1994), NDVI-derived land cover classification at a global scale, *Int. J. Remote Sens.*, *15*, 3567–3586.

Duce, R. A. (1995), Sources, distributions, and fluxes of mineral aerosols and their relationship to climate, in *Aerosol Forcing of Climate*, edited by R. J. Charlson and J. Heintzenberg, pp. 43–72, John Wiley, Hoboken, N. J.

Fujita, S., A. Takahashi, J. H. Weng, L. F. Huang, H. K. Kim, C. K. Li, F. Huang, and F. T. Jeng (2000), Precipitation chemistry in East Asia, *Atmos. Environ.*, *34*, 525–537.

Gillette, D. A., and R. Passi (1988), Modeling dust emission caused by wind erosion, *J. Geophys. Res.*, *93*, 14,233–14,242.

Giorgi, F. (1986), A particle dry-deposition parameterization scheme for use in tracer transport models, *J. Geophys. Res.*, *91*, 9794–9806.

Giorgi, F. (1988), Dry deposition velocities of atmospheric aerosols as inferred by applying a particle deposition parameterization to a general circulation model, *Tellus, Ser. B*, *40*, 23–41.

Gong, S. L., L. A. Barrie, and J. P. Blanchet (1997a), Modeling sea-salt aerosols in the atmosphere: 1. Model development, *J. Geophys. Res.*, *102*, 3805–3818.

Gong, S. L., L. A. Barrie, J. M. Prospero, D. L. Savoie, G. P. Ayers, J. P. Blanchet, and L. Spacek (1997b), Modeling sea-salt aerosols in the atmosphere: 2. Atmospheric concentrations and fluxes, *J. Geophys. Res.*, *102*, 3819–3830.

Gong, S. L., X. Zhang, T. Zhao, I. G. Mckendry, D. A. Jaffe, and N. Lu (2003), Characterization of soil dust aerosol in China and its transport and distribution during 2001 ACE-Asia: 2. Model simulation and validation, *J. Geophys. Res.*, *108*(D9), 4262, doi:10.1029/2002JD002633.

In, H. J., and S. U. Park (2002), A simulation of long-range transport of yellow sand observed in April 1998 in Korea, *Atmos. Environ.*, *36*, 4173–4187.

In, H. J., and S. U. Park (2003), The soil particle size dependent emission parameterization for an Asian dust (yellow sand) observed in Korea in April 2002, *Atmos. Environ.*, *37*, 4625–4636.

Liu, M. L., D. L. Westphal, S. G. Wang, A. Shimizu, N. Sugimoto, J. Zhou, and Y. Chen (2003), A high-resolution numerical study of the Asian dust storms of April 2001, *J. Geophys. Res.*, *108*(D23), 8653, doi:10.1029/2002JD003178.

Marticorena, B., and G. Bergametti (1995), Modeling the atmospheric dust cycles: 1. Design of a soil-derived dust emission scheme, *J. Geophys. Res.*, *100*, 16,415–16,430.

Monahan, E. C., D. E. Spiel, and K. L. Davidson (1986), A model of marine aerosol generation via white caps and wave disruption, in *Oceanic Whitecaps*, pp. 167–174, D. Reidel, Norwell, Mass.

Mori, I., M. Nishikawa, H. Quan, and M. Morita (2002), Estimation of the concentration and chemical composition of kosa aerosols at their origin, *Atmos. Environ.*, *36*, 4569–4575.

Mori, I., M. Nishikawa, T. Tanimura, and H. Quan (2003), Change in size distribution and chemical composition of Kosa (Asian dust) aerosol during long-range transport, *Atmos. Environ.*, *37*, 4253–4263.

Park, S. U., and H. J. In (2003), Parameterization of dust emission for the simulation of the yellow sand (Asian dust) event observed in March 2002 in Korea, *J. Geophys. Res.*, *108*(D19), 4618, doi:10.1029/2003JD003484.

Sehmel, G. A. (1980), Particle and gas dry deposition, *Atmos. Environ.*, *14*, 983–1011.

Seinfeld, J. H., and S. N. Pandis (1998), *Atmospheric Chemistry and Physics: From Air Pollution to Climate Change*, John Wiley, Hoboken, N. J.

Shao, Y., X. Tang, J. Li, K. Li, and S. Yuan (1995), The application of accelerator mass spectrometry (AMS) in the study of source identification of aerosols in China, *Pure Appl. Chem.*, *67*, 1457–1459.

Shao, Y. (2001), A model of mineral dust emission, *J. Geophys. Res.*, *106*, 20,239–20,254.

Shao, Y. P., et al. (2003), Northeast Asian dust storms: Real-time numerical prediction and validation, *J. Geophys. Res.*, *108*(D22), 4691, doi:10.1029/2003JD003667.

Slinn, W. G. N. (1982), Prediction for particle deposition to vegetative surfaces, *Atmos. Environ.*, *16*, 1785–1794.

Slinn, W. G. N. (1984), Precipitation scavenging, in *Atmospheric Science and Power Production*, pp. 466–532, Tech. Inf. Cent., Off. of Sci. and Technol. Inf., Dep. of Energy, Washington, D. C.

Sokolic, I. N., O. B. Toon, and R. W. Bergstrom (1998), Modeling of radiative characteristics of airborne mineral aerosols at infrared wavelengths, *J. Geophys. Res.*, *103*, 8813–8826.

Song, C. H., and G. R. Carmichael (2001), A three-dimensional modeling investigation of the evolution processes of dust and sea-salt particles in East Asia, *J. Geophys. Res.*, *106*, 18,131–18,154.

Tegen, I., and I. Fung (1994), Modeling of mineral dust in the atmosphere: Sources, transport, and optical thickness, *J. Geophys. Res.*, *99*, 22,897–22,914.

Uno, I., H. Amano, S. Emori, K. Kinoshita, I. Matsui, and N. Sugimoto (2001), Transpacific yellow sand transport observed in April 1998, *J. Geophys. Res.*, *106*, 18,331–18,344.

van den Berg, A., F. Dentener, and J. Lelieveld (2000), Modeling the chemistry of the marine boundary layer: Sulphate formation and the role of sea-salt aerosol particles, *J. Geophys. Res.*, *105*, 11,671–11,698.

Walcek, C. J., and N. M. Aleksic (1998), A simple but accurate mass conservative peak-preserving, mixing ratio bounded advection algorithm with Fortran code, *Atmos. Environ.*, *32*, 3863–3880.

Wang, W., and T. Wang (1996), On acid rain formation in China, *Atmos. Environ.*, *30*, 4091–4093.

Wang, Z. F., H. Ueda, and M. Y. Huang (2000), A deflation module for use in modeling long-range transport of yellow sand over East Asia, *J. Geophys. Res.*, *105*, 26,947–26,958.

Westphal, D. L., O. B. Toon, and T. N. Carlson (1987), A two-dimensional investigation of the dynamics and microphysics of Saharan dust storms, *J. Geophys. Res.*, *92*, 3027–3049.

Westphal, D. L., O. B. Toon, and T. N. Carlson (1988), A case study of mobilization and transport of Saharan dust, *J. Atmos. Sci.*, *45*, 2145–2175.

Zhang, D. Z., J. Zang, G. Y. Shi, Y. Iwasaka, A. Matsuki, and D. Trochkine (2003), Mixture state of individual Asian dust particles at a coastal site of Qingdao, China, *Atmos. Environ.*, *37*, 3895–3901.

Zhang, L. M., S. L. Gong, J. Padro, and L. Barrie (2001), A size-segregated particle dry deposition scheme for an atmospheric aerosol module, *Atmos. Environ.*, *35*(3), 549–560.

Zhang, R. J., M. X. Wang, X. Y. Zhang, and G. H. Zhu (2003), Analysis on the chemical and physical properties of particles in a dust storm in spring in Beijing, *Powder Technol.*, *137*, 77–82.

Zhang, X. Y., R. Arimoto, G. H. Zhu, T. Chen, and G. Y. Zhang (1998), Concentration, size-distribution, and deposition of mineral aerosol over Chinese desert regions, *Tellus, Ser. B*, *50*, 317–331.

Zhang, X. Y., S. L. Gong, Z. X. Shen, F. M. Mei, X. X. Xi, L. C. Liu, Z. J. Zhou, D. Wang, Y. Q. Wang, and Y. Cheng (2003), Characterization of soil dust aerosol in China and its transport and distribution during 2001 ACE-ASIA: Network observations, *J. Geophys. Res.*, *108*(D9), 4261, doi:10.1029/2002JD002632.

Zhao, Y. L., S. L. Gong, X. Y. Zhang, and I. G. Mckendry (2003), Modeled size-segregated wet and dry deposition budgets of soil dust aerosol during ACE-ASIA 2001: Implications for transpacific transport, *J. Geophys. Res.*, *108*(D23), 8665, doi:10.1029/2002JD003363.

────────────────

K. Arao, Faculty of Environmental Sciences, Nagasaki University, 852-8521 Nagasaki, Japan.

Z. Han, H. Hasome, and K. Matsuda, Acid Deposition and Oxidant Research Center (ADORC), 950-2144 Niigata-shi, Japan. (han@adorc.gr.jp)

Y. Kanai, National Institute of Advanced Industrial Science and Technology, 305-8567 Tsukuba, Japan.

H. Ueda, Disaster Prevention Research Institute, Kyoto University, Uji, 611-0011 Kyoto, Japan.
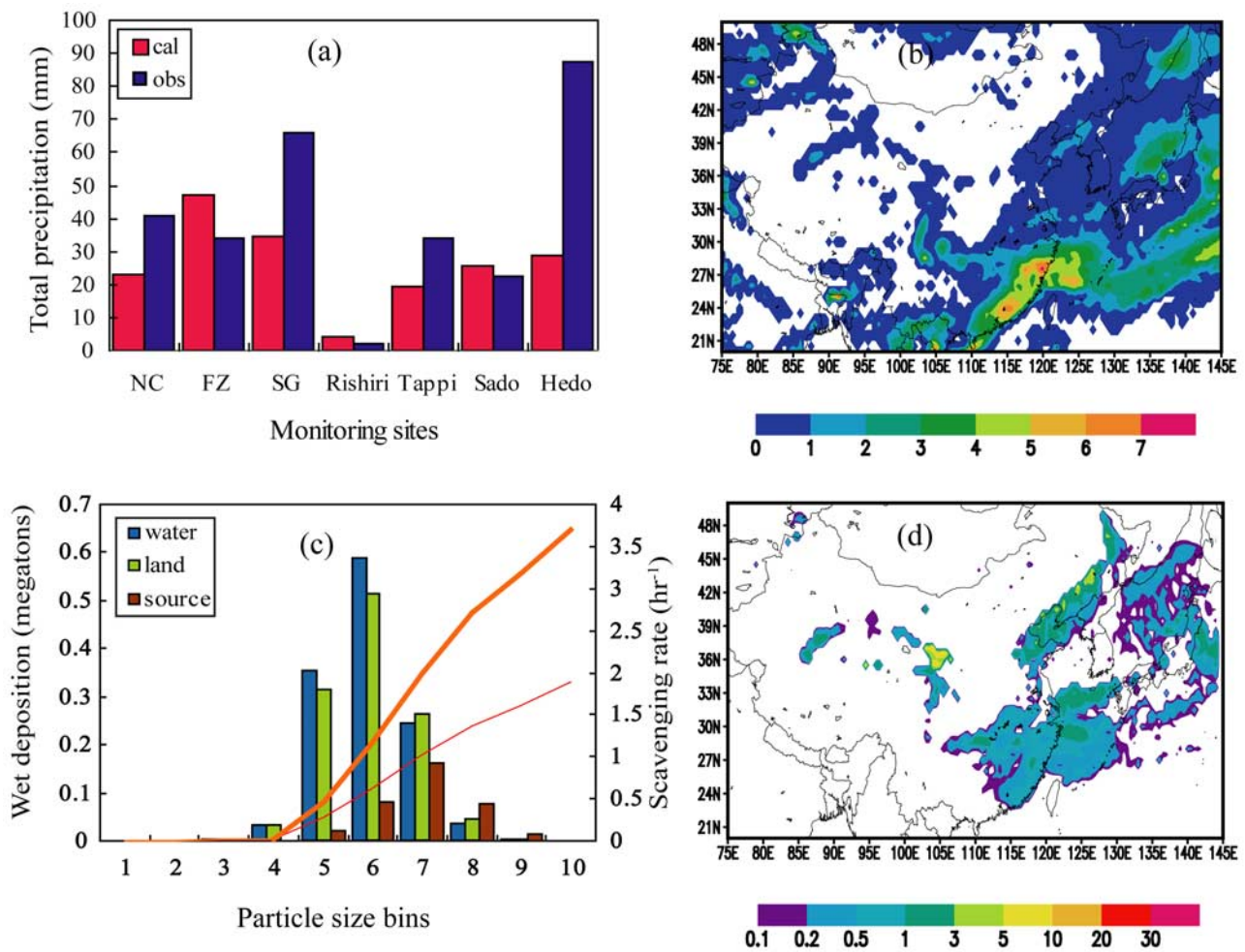
R. Zhang, Institute of Atmospheric Physics, Chinese Academy of Sciences, 100029, Beijing, China.
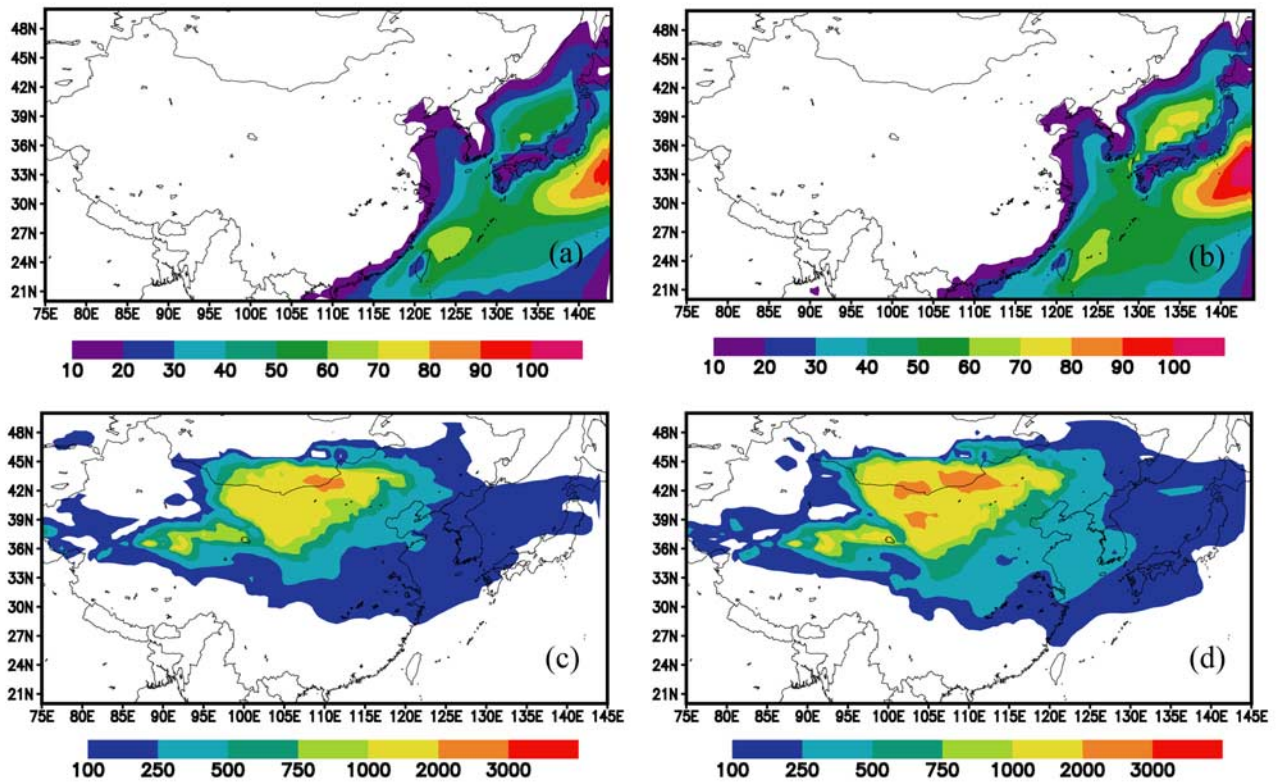
Figure 11. Average surface sea salt concentrations (μg m^{-3}) for the period of (a) 15–24 March and (b) 19–23 March, and average surface dust concentrations (μg m^{-3}) for the period of (c) 15–24 March and (d) 19–23 March 2002.
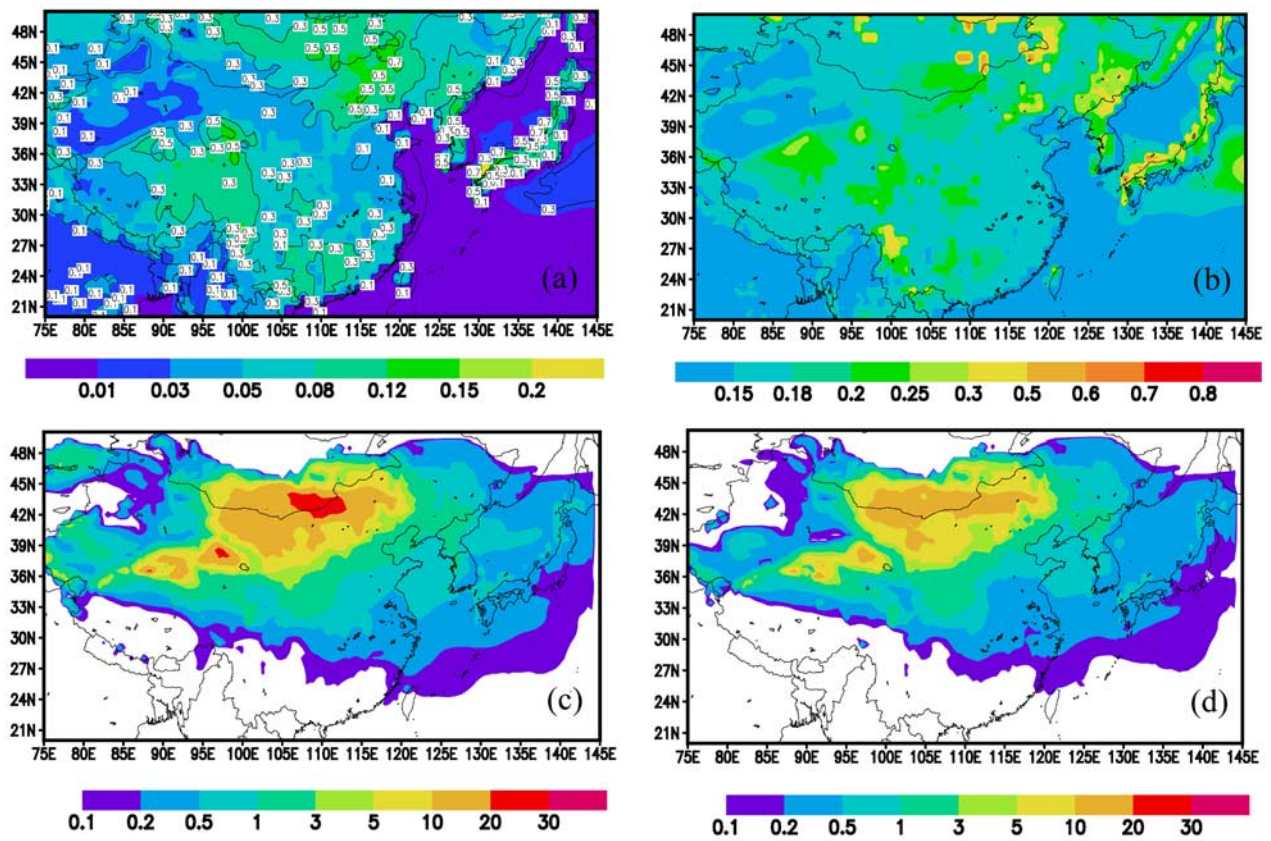
Figure 16. Spatial distribution of averages of (a) friction velocity (m s^{-1}) and particle Vd (cm s^{-1}) for a size of 0.84 μm, (b) Vd (cm s^{-1}) for a size of 4 μm, (c) total dry deposition (g m^{-2}) for the period of 15–24 March, and (d) total dry deposition (g m^{-2}) for the period of 19–23 March 2002.

Figure 17. (a) Simulated and observed total precipitation (mm) at seven monitoring sites, (b) simulated distribution of total precipitation in the domain (cm), (c) bin resolved dust wet deposition (megatons) (for three kinds of underlying surfaces) and scavenging rate (hour^{-1}) under the precipitation rate of 1 mm h^{-1} (thin line) and 3 mm h^{-1} (thick line), and (d) total wet deposition of soil dust (g m^{-2}) in the domain for the period of 15–24 March 2002.